UNIVERSIDADE DE BRASÍLIA

INSTITUTO DE FÍSICA

JULIANA DOS ANJOS RIBEIRO DOS SANTOS

FMR STUDY OF THE EXCHANGE BIAS EFFECT AS A FUNCTION OF RU LAYER'S THICKNESS IN SI/RU/IRMN/CO/RU(X)/PY/IRMN/RU MULTILAYERS

ESTUDO POR FMR DA DEPENDÊNCIA DO EFEITO EXCHANGE BIAS EM FUNÇÃO DA ESPESSURA DE RU(X) EM FILMES MULTICAMADAS DE SI/RU/IRMN/CO/RU(X)/PY/IRMN/RU

BRASÍLIA

21 DE JANEIRO DE 2026

Juliana dos Anjos Ribeiro dos Santos

FMR study of the Exchange Bias effect as a function of Ru layer's thickness in Si/Ru/IrMn/Co/Ru(x)/Py/IrMn/Ru multilayers

Estudo por FMR da dependência do efeito exchange bias em função da espessura de Ru(x) em filmes multicamadas de Si/Ru/IrMn/Co/Ru(x)/Py/IrMn/Ru

Estudo por FMR da dependência do efeito exchange bias em função da espessura de Ru(x) em filmes multicamadas de Si/-Ru/IrMn/Co/Ru(x)/Py/IrMn/Ru

Dissertação apresentada ao Instituto de Física da Universidade de Brasília como parte dos requisitos necessários à obtenção do título de Mestre em Física.

Orientador: Prof. Dr. Paulo Eduardo Narcizo de Souza

Universidade de Brasília – UnB

Instituto de Física

Brasília

21 de janeiro de 2026

Ficha catalográfica elaborada automaticamente,
com os dados fornecidos pelo(a) autor(a)

dos Anjos Ribeiro dos Santos, Juliana
dD722ee Estudo por FMR da dependência do efeito exchange bias em função da espessura de Ru(x) em filmes multicamadas de Si/Ru/IrMn/Co/Ru(x)/Py/IrMn/Ru / Juliana dos Anjos Ribeiro dos Santos; orientador Paulo Eduardo Narcizo de Souza. Brasília, 2026.
94 p.

Dissertação(Mestrado em Física) Universidade de Brasília, 2026.

1. FMR. 2. Ressonância ferromagnética. 3. Exchange bias. 4. Filmes finos. I. Narcizo de Souza, Paulo Eduardo, orient. II. Título.

Juliana dos Anjos Ribeiro dos Santos

FMR study of the Exchange Bias effect as a function of Ru layer's thickness in Si/Ru/IrMn/Co/Ru(x)/Py/IrMn/Ru multilayers

Estudo por FMR da dependência do efeito exchange bias em função da espessura de Ru(x) em filmes multicamadas de Si/Ru/IrMn/Co/Ru(x)/Py/IrMn/Ru

Estudo por FMR da dependência do efeito exchange bias em função da espessura de Ru(x) em filmes multicamadas de Si/-Ru/IrMn/Co/Ru(x)/Py/IrMn/Ru

Dissertação apresentada ao Instituto de Física da Universidade de Brasília como parte dos requisitos necessários à obtenção do título de Mestre em Física.

Trabalho aprovado. Brasília, 21 de janeiro de 2026:

Prof. Dr. Paulo Eduardo Narcizo de Souza
UnB

Prof. Dr. Edmilson Felix da Silva
UFRN

Prof. Dr. Fermin Fidel Herrera Aragon
UnB

Brasília
21 de janeiro de 2026

À minha mãe, pelo apoio incondicional que tornou esta conquista possível.

Agradecimentos

A realização deste trabalho só foi possível graças ao apoio e incentivo de diversas pessoas e instituições, às quais expresso minha sincera gratidão.

Primeiramente, agradeço ao meu orientador, Paulo Souza, pela orientação, pela confiança e pelas palavras de incentivo ao longo dos últimos anos. Seu apoio foi essencial para o desenvolvimento desta pesquisa e para a minha formação profissional.

Agradeço também aos professores Márcio Solino e Marcos Sousa, pelas sugestões valiosas e pela disponibilidade.

Agradeço aos meus queridos amigos que, pela companhia e pelo carinho, tornaram essa jornada mais leve. Em especial, agradeço ao Lucca e à Laura, que compartilharam as especificidades desse desafio e não faltaram com suporte e momentos incríveis.

Sou profundamente grata à minha família, principalmente minha mãe, Márcia, pelo amor, paciência e incentivo incondicional. Sem o apoio de vocês, nada disso seria possível.

Por fim, agradeço à CAPES pelo apoio financeiro que viabilizou o desenvolvimento deste trabalho e à UnB pelas oportunidades acadêmicas e qualidade de ensino.

"Some consider doubt a weakness, but for me it is far healthier than certainty, although it does need to be seen as something open and flexible, not disabling. As has often been said, certainty rather than doubt is the opposite of faith."

- Jocelyn Bell Burnell

Resumo

Filmes magnéticos finos são materiais bidimensionais cujas propriedades magnéticas diferem significativamente daquelas de seus correspondentes volumétricos. A principal motivação para seu estudo reside em seu potencial de aplicação em tecnologias avançadas de armazenamento de dados, em particular na gravação magnética. Este trabalho utiliza filmes multicamadas do tipo Si/Ru/IrMn/Co/Ru(x)/Py/IrMn/Ru. A interação magnética entre as camadas ferromagnéticas (Co e Py) e as camadas antiferromagnéticas de IrMn deve se manifestar por meio do efeito de exchange bias, caracterizado por um deslocamento assimétrico do ciclo de histerese M×H ao longo do eixo do campo magnético. A técnica de espectroscopia de ressonância ferromagnética (FMR) é amplamente consolidada para a determinação dos principais parâmetros de sistemas magnéticos e facilita a investigação de camadas acopladas, permitindo medições precisas de parâmetros fundamentais, como as constantes de anisotropia. Nesse contexto, este estudo emprega a técnica de FMR para examinar o efeito da espessura da camada central de Ru(x) sobre o efeito de exchange bias nas multicamadas mencionadas. Por meio da investigação sistemática da dependência angular dos campos de ressonância no plano do filme, foram encontradas evidências claras da presença de anisotropia magnética unidirecional no plano em todos os filmes investigados, bem como uma dependência complexa e não monótona do exchange bias com a espessura do espaçador Ru(x).

Palavras-chaves: FMR, Ressonância ferromagnética, Exchange bias, Filmes finos.

Abstract

Magnetic thin films are two-dimensional materials with magnetic properties that differ greatly from their bulk counterparts. Their primary investigation motivation lies in their potential application in advanced data storage technology, particularly magnetic recording. This study employs Si/Ru/IrMn/Co/Ru(x)/Py/IrMn/Ru multilayer films. The magnetic interaction between the ferromagnetic layers (Co and Py) and antiferromagnetic IrMn layers is expected to manifest itself in the exchange bias effect, which is characterized by an asymmetric displacement in the hysteresis MxH loop along the magnetic field axis. The ferromagnetic resonance spectroscopy (FMR) technique is well established for determining the main parameters of magnetic systems and facilitates the investigation of coupled layers, providing precise measurements of key parameters like anisotropy constants. In that sense, this study employs FMR to examine the effect of the Ru(x) central layer's thickness on the exchange bias effect of the previously mentioned multilayer films. By systematically probing the angular dependence of the in-plane resonance fields, we found clear evidence of an in-plane unidirectional magnetic anisotropy in all films investigated, along with a complex, non-monotonic dependence of the exchange bias on the Ru(x) spacer thickness.

Key-words: FMR, Ferromagnetic resonance, Exchange bias, Thin films.

List of Figures

List of Tables

List of abbreviations and acronyms

CAPES	Coordenação de Aperfeiçoamento de Pessoal de Nível Superior
IF	Instituto de Física
UnB	Universidade de Brasília
FMR	Ferromagnetic resonance
GMR	Giant magnetoresistance
EB	Exchange bias
FM	Ferromagnetic
AFM	Antiferromagnetic
MRAM	Magnetoresistive random-access memory
VSM	Vibrating sample magnetometer
SI	International System of Units (*Système International*)
cgs	Centimeter-Gram-Second system of units
RKKY	Ruderman-Kittel-Kasuya-Yosida interaction
EPR	Electron Paramagnetic Resonance
NMR	Nuclear Magnetic Resonance
DC	Direct current
RF	Radio frequency
CBPF	Centro Brasileiro de Pesquisas Físicas
GIXD	Grazing-Incidence X-ray Diffraction
XRD	Conventional X-ray Diffraction
TEM	Transmission Electron Microscopy
SEM	Scanning Electron Microscopy
FAPERJ	Fundação de Amparo à Pesquisa do Estado do Rio de Janeiro
MBE	Molecular beam epitaxy

List of symbols

M	magnetization
H	magnetic field
μ	magnetic moment
I	electric current
dA	infinitesimal area element
$d\mu$	infinitesimal magnetic moment element
L	orbital angular momentum
μ_l	orbital magnetic moment
S	spin
J	total angular momentum
μ_l	total magnetic moment
l	orbital quantum number
e	electron charge
m_e	electron mass
μ_B	Bohr magneton
γ	gyromagnetic ratio
g	Landé g-factor
B	magnetic induction
μ_0	permeability of free space
χ	magnetic susceptibility
M_s	saturation magnetization
M_r	remanent magnetization
H_c	coercive field

ψ	wave function
E	energy
H	Hamiltonian
Je	exchange constant
r	distance
Z	number of conduction electrons per atom
N	density of states
ϵ_F	Fermi level energy
k_F	Fermi wave vector
ε	energy density
A	exchange stiffness
V	volume
K_1	first order cubic anisotropy constant
K_2	second order cubic anisotropy constant
K_u	uniaxial anisotropy constant
K_s	surface anisotropy constant
t	thickness
λ	magnetostriction constant
σ	stress
T	temperature
T_N	Néel temperature
T_C	Curie temperature
H_{ex}	exchange bias field from magnetization measurement
h	microwave magnetic field
$\mathcal{N}$	demagnetizing tensor
ω	frequency of the microwave magnetic field

H_{res}	FMR resonance field
H_{eb}	exchange bias field from FMR
$\hbar$	(Planck constant)/(2π)

Contents

Introduction

The first documentation of inorganic thin films dates back to the Egyptians, who produced gold layers with thickness below approximately 3000Å more than 5000 years ago. With advances in scientific knowledge and technology, thin film production has come a long way toward the expanding field it is today (OHRING, 2001; GREENE, 2014).

In a contemporary context, magnetic thin films have been studied and employed in magnetic recording technologies due to the increasing demand for high storage densities and for the thermal stability of recorded information (MOSER et al., 2002). The discovery of the giant magnetoresistance (GMR) effect, characterized by a significant change in electrical resistance depending on the relative orientation of magnetization, propelled research on magnetic multilayer films and facilitated their application in magnetic sensors and hard-disk read heads (ENNEN et al., 2016).

The exchange bias effect (EB), caused by interface exchange coupling of ferromagnetic (FM) and antiferromagnetic (AFM) medium, also plays an important role in the development of spintronic devices, as strong EB is directly associated with enhanced stability and energy efficiency. A prominent example of EB-based technology is the spin-valve system, widely used in magnetoresistive random-access memory (MRAM). Such systems use the GMR effect to modulate the resistance by controlling the magnetization direction of a free FM layer via an external magnetic field. This layer is separated from an exchange-biased AFM/FM bilayer by a non-magnetic spacer (HUANG et al., 2023; SUN et al., 2023; SOUSA, 2013). More recently, alternative multilayer and heterostructure configurations have been explored to employ EB effects for potential applications, including systems exhibiting both in-plane and perpendicular exchange bias (DONG et al., 2022; FAN et al., 2022; HUANG et al., 2021).

In this dissertation, thin film multilayers with two exchange-biased interfaces were studied in order to investigate the EB effect as a function of the nonmagnetic spacer layer's thickness. Si/Ru/IrMn/Co/Ru/Py/IrMn/Ru multilayers with varying central ruthenium layer thicknesses fabricated by magnetron sputtering were characterized by ferromagnetic resonance (FMR) measurements, which is a well-established technique for determining key magnetic parameters and probing coupled layers (LINDNER; BABERSCHKE, 2003). This dissertation investigates the exchange bias effect at the IrMn/Co and Py/IrMn interfaces of these structures. The advancement in knowledge of the exchange bias effect may contribute to the development of novel technologies.

The dissertation is organized as follows: Chapters 1 to 3 delve into the main theory relevant to the scope of this text. Chapter 1 introduces the magnetism of matter,

its origin, the different ways in which materials respond to applied magnetic fields and the main magnetic interactions. In Chapter 2, the particularities of magnetism in nanoscale materials and the main magnetic energies and interactions relevant to thin films are discussed. Chapter 3 describes the theory involving ferromagnetic resonance and the Smit-Suhl-Beljers approach for determining the resonance condition from the energy density expression of the film. Chapter 4 describes the experimental procedures. The deposition technique used for growing the films is explained, and the structural characterization techniques used are reported. The methodology of the magnetization measurements, including the FMR and VSM experiments, is also described. Finally, Chapter 5 presents the experimental results and discusses them, giving possible origins for the behavior observed for the exchange bias field of IrMn/Py and Co/IrMn interfaces.

Parte I

Fundamentals of Thin Film Magnetism and Ferromagnetic Resonance

1 The magnetism of matter

Magnetic materials were already recognized by the ancient Greeks, who knew that a piece of iron would become magnetized when rubbed with stones consisting of magnetite (Fe_3O_4) (BUSCHOW, 2003). Nevertheless, the origin of the magnetism of matter was only explained much later, with quantum mechanics. Currently, these materials play a central role in both fundamental physics and modern technologies, from data storage to spintronics. This chapter explores the fundamental aspects of the magnetism of matter.

1.1 Origin of magnetism of matter

Magnetic fields can be originated from electric currents and magnetized materials. The fundamental quantity to describe the atomic origin in solid-state magnetism is the magnetic moment μ (COEY, 2010). Classically, an electron moving around the nucleus can be viewed as follows: a current I around an elementary oriented loop $\mathbf{dA}$ (as in Figure 1) produces a magnetic moment $\mathbf{d}\boldsymbol{\mu}$, given by equation 1.1 and in units of Am^2 (SI) or emu (cgs). For a loop of finite size, the magnetic moment, which is analogous to a magnetic dipole, can be taken as equation 1.2 (BLUNDELL, 2001; WEI, 2015).

$$\mathbf{d}\boldsymbol{\mu} = I\mathbf{dA} \tag{1.1}$$

$$\boldsymbol{\mu} = \int \mathbf{d}\boldsymbol{\mu} = I \int \mathbf{dA} \tag{1.2}$$

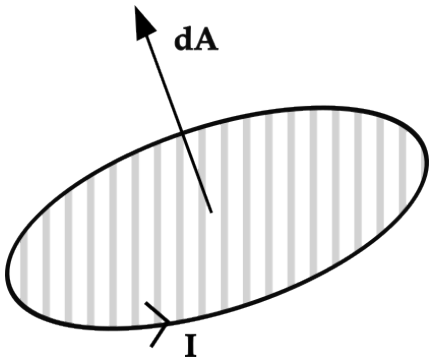

Figure 1 – Current loop.

Quantum mechanically, the magnetic moment $\boldsymbol{\mu}$ in atoms is further associated to the orbital angular momentum $\mathbf{L}$ of the electron and its spin $\mathbf{S}$ (COEY, 2010). The magnetic moment associated with the angular momentum $\boldsymbol{\mu}_l$ of an electron is given by equation 1.3, with magnitude given by equation 1.4.

$$\boldsymbol{\mu_l} = -\frac{e}{2m_e}\hbar\mathbf{L}, \tag{1.3}$$

$$|\boldsymbol{\mu_l}| = \mu_B\sqrt{l(l+1)}, \tag{1.4}$$

where $\mu_B = \frac{e\hbar}{2m_e}$ is the Bohr magneton, e is the electron charge and m_e is the electron mass.

Similarly, the spin magnetic moment is related to the spin angular momentum by equation 1.5

$$\boldsymbol{\mu_S} = -2\mu_B\mathbf{S}. \tag{1.5}$$

L and **S** combine to form the total angular momentum **J**.

$$\mathbf{J} = \mathbf{L} + \mathbf{S}. \tag{1.6}$$

The total magnetic moment parallel to **J** is given by equation 1.7, with magnitude given by equation 1.8

$$\boldsymbol{\mu_J} = -g\mu_B\mathbf{J} \tag{1.7}$$

$$|\boldsymbol{\mu_J}| = g\mu_B\sqrt{J(J+1)}, \tag{1.8}$$

where g is the Landé g-factor whose value depends on the material, according to 1.9 (GUIMARÃES; OLIVEIRA, 1998; BUSCHOW, 2003).

$$g = 1 + \frac{J(J+1+S(S+1)-L(L+1))}{2J(J+1)} \tag{1.9}$$

1.2 Magnetic response of materials

1.2.1 Magnetic induction and magnetization

A magnetic solid is composed of a large number of atoms, each possessing a magnetic moment. The total magnetic moment per unit volume is referred to as magnetization **M**.

$$\mathbf{M} = \frac{\sum \boldsymbol{\mu}}{V} \tag{1.10}$$

When an external magnetic field **H** is applied to the material, the resulting response is called magnetic induction **B**. The relationship between **B**, **H**, and **M** is given by

$$\mathbf{B} = \mu_{\mathbf{0}} \left(\mathbf{H} + \mathbf{M} \right), \tag{1.11}$$

where $\mu_0 = 4\pi \times 10^{-7} Hm^{-1}$ is the permeability of free space. The SI unit of B is tesla (T) and the cgs unit of B is gauss (G), with 1 T=10^4 G.(BLUNDELL, 2001; WEI, 2015).

1.2.2 Susceptibility

When a material is subjected to a varying external magnetic field, its response (the magnetization) also varies. The measure of the magnetic response of a medium to the action of a magnetic field is given by the magnetic susceptibility χ, defined by

$$\chi = \frac{M}{H}, \tag{1.12}$$

or in differential for, by $\chi = \frac{\partial M}{\partial H}$ (GUIMARÃES; OLIVEIRA, 1998).

1.2.3 Magnetic hysteresis

Hysteresis, from the Greek *hystérēsis* meaning "occurring late", is the phenomenon in which a system's response lags behind changes in the effect producing it, causing its state to depend on its history rather than only on current conditions (Collins Dictionary, 2024). In magnetic materials, the magnetization for a given magnetic field may depend not only on the field itself but also on the history of its variation, which means that the response of materials' magnetization to an applied magnetic field may not be reversible. The magnetic hysteresis loop, given by measurements of magnetization with varying external magnetic field, is the characteristic manifestation of this response. When the applied magnetic field is returned to zero after saturation, the magnetization decreases from its saturation value M_s to the remanent magnetization M_r. The magnitude of field required to reduce the magnetization to zero is defined as the coercive field, H_c, as seen in Figure 2. Moreover, the value of this coercive field can be used to classify magnetic materials as hard or soft magnets. Hard magnetic materials have high coercivity ($\sim 10^4$ Oe), which makes them suitable for permanent magnets. In contrast, soft magnetic materials exhibit low coercivity ($\sim 10^{-1}$ Oe) (WEI, 2015; COEY, 2010; MARKÓ, 2018).

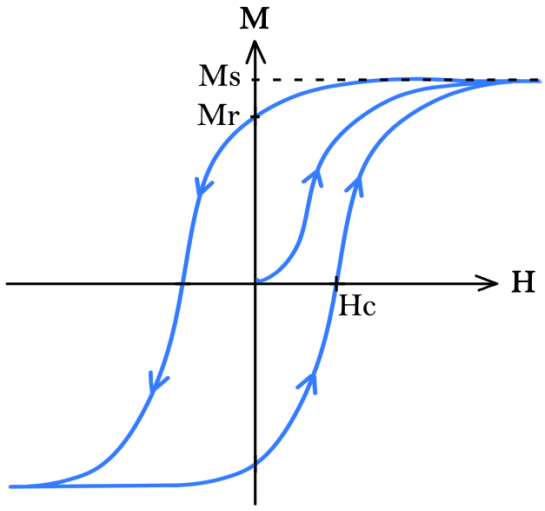

Figure 2 – Illustration of magnetic hysteresis MxH curve for a ferromagnet.

1.3 Magnetic ordering

Different materials respond differently to magnetic fields. That response classifies the material as diamagnetic, paramagnetic, ferromagnetic, antiferromagnetic, and ferrimagnetic materials. A representation of the arrangement of magnetic moments in each type of ordering is presented in Figure 3.

For a diamagnetic substance, a magnetic field induces a magnetic moment that opposes the applied magnetic field that caused it (BLUNDELL, 2001). From a classical viewpoint, when an external magnetic field is applied to an electrical circuit, it induces a current that opposes the original one, an effect consistent with Lenz's law. A similar phenomenon occurs for electrons orbiting within atoms: the induced current reduces the orbital magnetic moment, resulting in a negative magnetic susceptibility. As a result, all materials exhibit some degree of diamagnetism. However, only those in which this is the sole magnetic behavior are classified as diamagnetic materials. In the absence of an external magnetic field, the magnetic moments of individual atoms are randomly oriented, resulting in no net magnetization (GUIMARÃES; OLIVEIRA, 1998; WEI, 2015).

Paramagnetism is characterized by a positive magnetic susceptibility, meaning that an applied magnetic field induces a magnetization that tends to align parallel to the field. However, this susceptibility is typically small because thermal energy, which promotes random orientation of magnetic moments, is much greater than the magnetic energy trying to align them. In the absence of an external field, the atomic magnetic moments remain randomly oriented, resulting in no net magnetization (BLUNDELL, 2001; WEI, 2015).

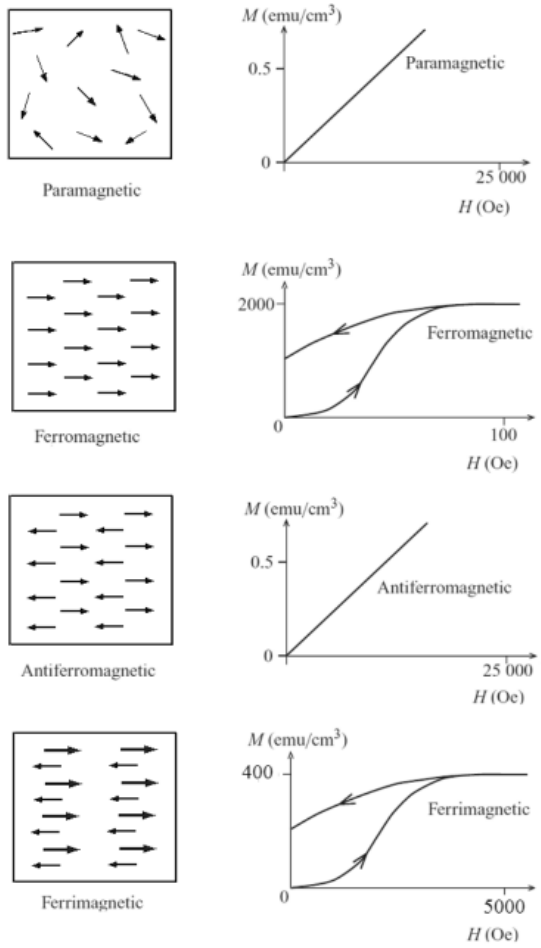

Figure 3 – Magnetic ordering and magnetization curves.(WEI, 2015)

In a ferromagnet, spontaneous magnetization occurs even without an external magnetic field because the magnetic moments of individual atoms align parallel to each other. This alignment typically follows the easy axes defined by the crystal structure. In 1907, Weiss first explained this behavior by proposing that each atomic moment experiences an effective magnetic field resulting from the influence of neighboring magnetic moments. When an external magnetic field is applied, ferromagnets exhibit a large and positive magnetic susceptibility (GUIMARÃES; OLIVEIRA, 1998; COEY, 2010; BLUNDELL, 2001; WEI, 2015).

In antiferromagnetic materials, the magnetic moments are aligned antiparallel to each other, resulting in no net magnetization. Typically, these systems can be considered as two interlaced sublattices (WEI, 2015; BLUNDELL, 2001).

Lastly, in ferrimagnetic materials, in contrast to the antiferromagnets, the magnetic moments of sublattices are not equivalent. There is antiferromagnetic (antiparallel) alignment. However, their differing magnitudes result in non-zero spontaneous magnetization. (BUSCHOW, 2003).

1.4 Magnetic interactions

1.4.1 Exchange interaction

The first modern theory of ferromagnetism was proposed by Pierre Weiss in 1906. In his theory, he introduced an internal molecular field within materials, which acts on each magnetic moment and is proportional to the magnetization of the ferromagnet. The Weiss molecular field originates from the exchange interaction, which arises from the Coulomb repulsion between two nearby electrons, typically in neighboring atoms, as well as from the Pauli exclusion principle, which forbids two electrons from occupying the same quantum state defined by a given set of quantum numbers (COEY, 2010). The exchange interaction is therefore at the root of the electronic magnetic phenomena in matter (BLUNDELL, 2001).

Considering a simple model of two electrons with spatial coordinates $\mathbf{r_1}$ and $\mathbf{r_2}$, in states $\psi_a(\mathbf{r_1})$ and $\psi_b(\mathbf{r_2})$, respectively, the total wavefunction of the system must be antisymmetric. Consequently, the spin part of the wavefunction must be a singlet state χ_S ($S = 0$), which is antisymmetric when the spatial part is symmetric, or a triplet state χ_T ($S = 1$), when the spatial part is antisymmetric. In this way, the wavefunctions for the singlet Ψ_S and triplet Ψ_T cases can be expressed as follows (BLUNDELL, 2001).

$$\begin{aligned}\Psi_S &= \frac{1}{\sqrt{2}}[\psi_a(\mathbf{r_1})\psi_b(\mathbf{r_2}) + \psi_a(\mathbf{r_2})\psi_b(\mathbf{r_1})]\chi_S \\ \Psi_T &= \frac{1}{\sqrt{2}}[\psi_a(\mathbf{r_1})\psi_b(\mathbf{r_2}) - \psi_a(\mathbf{r_2})\psi_b(\mathbf{r_1})]\chi_T.\end{aligned} \tag{1.13}$$

Assuming that the spin parts χ_S and χ_T are normalized, the energies of the two states are

$$\begin{aligned}E_S &= \int \Psi_S^* \hat{H} \Psi_S d\mathbf{r_1} d\mathbf{r_2} \\ E_T &= \int \Psi_T^* \hat{H} \Psi_T d\mathbf{r_1} d\mathbf{r_2},\end{aligned} \tag{1.14}$$

such that the energy difference between the states is

$$E_S - E_T = 2 \int \psi_a^*(\mathbf{r_1})\psi_b^*(\mathbf{r_2})\hat{H}\psi_a(\mathbf{r_2})\psi_b(\mathbf{r_1}) d\mathbf{r_1} d\mathbf{r_2}. \tag{1.15}$$

It is convenient to parameterize the energy difference between the singlet and triplet states using the electronic spin operators $\mathbf{S_1}$ and $\mathbf{S_2}$, as this simplifies the description of the energy of spin configurations in solids. Each electronic spin operator satisfies the relation $\mathbf{S_i}^2 = \frac{1}{2}\left(\frac{1}{2} + 1\right) = \frac{3}{4}$, so that the total spin $\mathbf{S}$ must satisfy (ASHCROFT; MERMIN, 1993)

$$\mathbf{S}^2 = (\mathbf{S_1} + \mathbf{S_1})^2 = \frac{3}{2} + 2\mathbf{S_1} \cdot \mathbf{S_2}. \tag{1.16}$$

Since $\mathbf{S}^2$ has the eigenvalue $S(S+1)$ in spin-S states, the operator $\mathbf{S_1} \cdot \mathbf{S_2}$ has the eigenvalue $-\frac{3}{4}$ in the singlet state and $\frac{1}{4}$ in the triplet state. Consequently, the Hamiltonian can be expressed in the form of an "effective Hamiltonian"

$$\hat{H} = \frac{1}{4}(E_S + 3E_T) - (E_S - E_T)\mathbf{S_1} \cdot \mathbf{S_2}. \tag{1.17}$$

By redefining the zero of energy and omitting the constant term $\frac{1}{4}(E_S + 3E_T)$, the spin-dependent effective Hamiltonian can be written as

$$\hat{H}_{spin} = -J_e \mathbf{S_1} \cdot \mathbf{S_2}, \tag{1.18}$$

where J_e is the exchange constant (or exchange integral), defined as

$$J_e = E_S - E_T = 2 \int \psi_a^*(\mathbf{r_1})\psi_b^*(\mathbf{r_2})\hat{H}\psi_a(\mathbf{r_2})\psi_b(\mathbf{r_1})d\mathbf{r_1}d\mathbf{r_2}. \tag{1.19}$$

If $J_e > 0$, $E_S > E_T$, and the triplet state ($S = 1$) is favored. Conversely, if $J_e < 0$, $E_S < E_T$, and the singlet state ($S = 0$) is favored.

Generalizing to neighboring atoms, one has

$$\hat{H} = -\sum_{ij} J_{e_{ij}} \mathbf{S_1} \cdot \mathbf{S_2}, \tag{1.20}$$

where $J_{e_{ij}}$ is the exchange constant between spins i and j, so that the Hamiltonian represents the coupling between these spins (BLUNDELL, 2001; MYDOSH, 1993).

1.4.2 Ruderman-Kittel-Kasuya-Yosida (RKKY) interaction

Ruderman, Kittel, Kasuya, and Yosida showed that a single magnetic impurity in a non-magnetic metal creates a non-uniform oscillatory spin polarization in the conduction band that decays with r^3 , leading to a long-range oscillatory coupling between localized spins at a distance r. The interaction is indirect because it does not involve direct coupling between magnetic moments and is called the RKKY interaction, or indirect exchange interaction (COEY, 2010; BLUNDELL, 2001).

The hamiltonian of the interaction is given by $H = J(r)\mathbf{S_i} \cdot \mathbf{S_j}$, with

$$J(r) = 6\pi Z J_e^2 N(\epsilon_F) \left[\frac{sin(2k_F r)}{(2k_F r)^4} - \frac{cos(2k_F r)}{(2k_F r)^3} \right], \tag{1.21}$$

where Z is the number of conduction electrons per atom, J_e is the exchange constant, $N(\epsilon_F)$ is the density of states at the Fermi level, k_F is the Fermi wave vector, and r is the distance between the impurities. The RKKY function, given by equation 1.21 $F(\xi)$, with $\xi = 2k_F r$, is shown in Figure 4 and illustrates the behavior of the interaction as a function of distance. It is worth noting the sign change of the function depending on the distance, indicating a variation between ferromagnetic coupling ($J_e > 0$) and antiferromagnetic coupling ($J_e < 0$). For large distances, the expression is reduced to (MYDOSH, 1993)

$$J(r) = \frac{J_0 cos(2k_F r + \phi)}{(2k_F r)^3}. \tag{1.22}$$

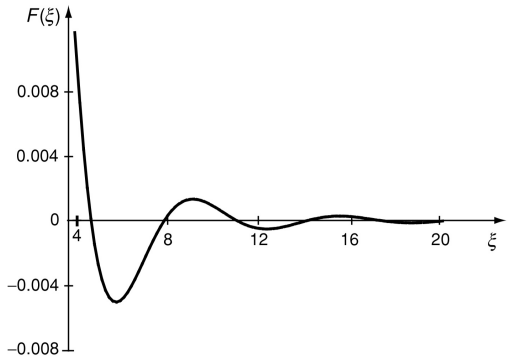

Figure 4 – RKKY function $F(\xi)$, from (COEY, 2010).

1.4.3 Dipolar interaction

The interaction between two magnetic dipoles $\mu_\mathbf{1}$ and $\mu_\mathbf{2}$ separated by a distance $\mathbf{r}$ is related to the force and torque they exert on each other. This interaction is direct anisotropic and long-range and its energy is given by equation 1.23 (BLUNDELL, 2001; WEI, 2015).

$$E_{dip} = \frac{\mu_0}{4\pi r^3}\left(\mu_\mathbf{1} \cdot \mu_\mathbf{2} - \frac{3}{r^2}(\mu_\mathbf{1} \cdot r)(\mu_\mathbf{2} \cdot \mathbf{r})\right) \tag{1.23}$$

While insufficient to account for magnetic ordering in the majority of materials, the dipolar interaction is a significant factor in the properties of systems with ordering temperatures in the milliKelvin range (BLUNDELL, 2001).

1.5 Anisotropy

Magnetic anisotropy is the characteristic that a magnetic material may posses if its internal energy depends on the direction of its magnetization with respect to the crys-

tallographic axes (BUSCHOW, 2003). Ferromagnetic single crystals, for example, exhibit "easy"and "hard" directions of the magnetization, which is a sufficient evidence of magnetic anisotropy (JOHNSON et al., 1996). Magnetic anisotropy can also be demonstrated by measurements of magnetization along a material's hard and an easy axis, as shown in Figure 5. The difference between the curves is due to the external extra field needed to saturate the magnetization along the hard axis. The magnetic anisotropy energy is numerically equal to the area enclosed between the two magnetization curves (POULOPOULOS; BABERSCHKE, 1999).

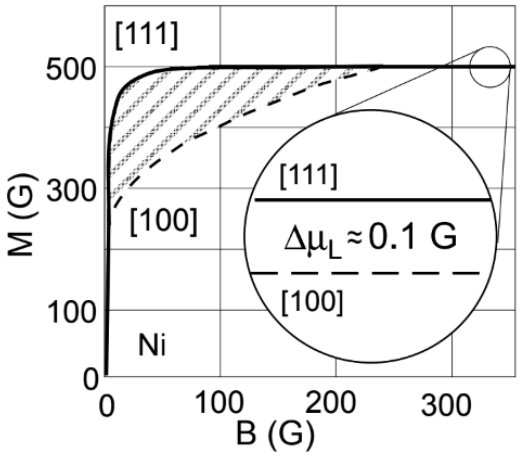

Figure 5 – Magnetization curves for the easy [111] and hard [100] axes of bulk Ni (POULOPOULOS; BABERSCHKE, 1999).

From a technological perspective, magnetic anisotropy is one of the most important properties of magnetic materials. Materials with high, medium, or low magnetic anisotropy may be suitable for different applications: in permanent magnets, data storage media, magnetic cores in transformers, or magnetic recording heads (JOHNSON et al., 1996).

In general, magnetic anisotropies are the evidence of broken symmetries in the lattice of any magnetic sample, since in a higher-symmetry configuration all directions are equivalent. (BUSCHOW, 2005; BLUNDELL, 2001) The microscopical origin of anisotropy is the dipole-dipole interaction and the spin orbit coupling. Both interactions couple the spin vectors to the lattice. However, the spin-orbit coupling plays a bigger role because it couples the spin to the charge (orbital) density distribution in the crystal (FARLE, 1998). The dipolar interaction, due to its long range property, typically introduces a shape-dependent contribution. This effect is especially significant in thin films and plays a major role in the commonly observed in-plane magnetization (JOHNSON et al., 1996). In thin films, a preferred orientation may be rooted in different factors from the bulk. The presence of symmetry-breaking elements, such as planar interfaces and surfaces, is a key component for this behavior (JOHNSON et al., 1996; FARLE, 1998).

2 Thin film magnetism

Materials behave differently from their bulk counterparts when their dimensions are reduced to the nanoscale. If the material has at least one dimension in the nanometer range, typically below 100 nanometers, it is considered a nanomaterial. The one small dimension class of materials is well represented by thin films. Two small dimensions make up the nanowire class, and three small dimensions define the nanoparticles (COEY, 2010). At these scales, surface effects become increasingly significant due to the high surface-to-volume ratio, which can strongly influence magnetic interactions. Magnetic properties that are altered at the nanoscale include remanence, exchange averaging of anisotropy, coercivity and the emergence of giant magnetoresistance and superparamagnetism (CULLITY; GRAHAM, 2011; COEY, 2010).

The phenomenon of superparamagnetism provides a clear and well-established example of how magnetic properties are affected by particle size reduction in nanoscale systems. In very small ferromagnetic particles, the formation of magnetic domains, which are regions within a magnetic material where the magnetic moments are aligned in the same direction, becomes energetically unfavorable, leading to the formation of single-domain. When these single-domain nanoparticles are dispersed in a nonmagnetic matrix and spaced far enough to prevent interaction, thermal fluctuations dominate their magnetic response and the system behaves like a paramagnet, even though the individual particles are ferromagnetic (BLUNDELL, 2001).

Magnetic thin films are two-dimensional materials that, because of their low dimensionality, present intrinsic magnetic properties that may differ from bulk materials. Many of these differences arise from the unique environments experienced by surface and interface atoms, as well as from strain effects induced by the underlying substrate. Such films, with thicknesses ranging from a single monolayer to over 100 nm, can be grown on crystalline or amorphous substrates using a variety of physical and chemical deposition techniques. The primary motivation for their investigation originates from their technological potential, particularly in the field of magnetic data storage and recording (COEY, 2010; OHRING, 2001; POULOPOULOS; BABERSCHKE, 1999). In the sections that follow, this chapter introduces the key theoretical concepts underlying magnetism in thin films, providing the necessary background for the discussions in the subsequent chapters.

2.1 Magnetic energies and anisotropy

The domain structure of ferromagnets and ferrimagnets results from free-energy minimization. A sufficiently strong applied field eliminates this structure, while reducing

the field leads to domain reformation. (COEY, 2010) The total magnetic energy density of a thin film is given by the sum of energy terms, each corresponding to an interaction to which the film is susceptible (WEI, 2015). The most common energy contributions in thin films are the following:

2.1.1 Exchange energy

As priory discussed, the existence of long-range magnetic ordering is often associated with the presence of an internal magnetic field, which is caused by the exchange interaction (BUSCHOW, 2003; COEY, 2010). In that sense, exchange interactions are fundamental to the emergence of such magnetic order (BLUNDELL, 2001). These interactions reflect both the Coulomb repulsion of two neighboring electrons and the Pauli exclusion principle, which prohibits them from sharing the same quantum state (COEY, 2010). As for the energy associated with the exchange interaction, it is given by

$$E_{ex} = -\sum_{ij} J_{e_{ij}} \left(\mathbf{S_i} \cdot \mathbf{S_j}\right), \tag{2.1}$$

where $J_{e_{ij}}$ is the exchange integral, $\mathbf{S_i}$ and $\mathbf{S_j}$ are vectors pointing along the directions of the magnetic moments of atoms i and j, respectively, and the summation usually occurs only to the nearest neighbors. A positive $J_{e_{ij}}$ indicates ferromagnetic behavior, while a negative $J_{e_{ij}}$ indicates antiferromagnetism (WEI, 2015).

Classically, the exchange energy density is expressed as

$$\varepsilon_{ex} = \frac{A}{V} \int dV \left(\nabla \frac{\mathbf{M}}{M_s}\right)^2, \tag{2.2}$$

where V is the volume of the material, A is the exchange stiffness and M_s is the saturation magnetization (WEI, 2015).

2.1.2 Zeeman energy

When a material with magnetization $\mathbf{M}$ is subjected to an external magnetic field $\mathbf{H_{ext}}$, it exerts a torque on the magnetic moments, tending to align them parallel to the field direction. This interaction is associated with the Zeeman energy. The energy density is given by

$$\varepsilon_{zee} = -\frac{\mu_0}{V} \int dV \mathbf{M} \cdot \mathbf{H_{ext}}, \tag{2.3}$$

and is minimized by aligning the magnetization along the external field (WEI, 2015).

2.1.3 Demagnetizing or shape anisotropy energy

The demagnetizing (or shape) anisotropy energy originates from the long-range magnetic dipolar interaction. The net magnetic dipoles, located at the boundaries of the material, tend to minimize the magnetostatic energy by creating this demagnetizing energy (PESSOA, 2010). This energy is also called shape anisotropy because the dipolar interaction "senses" the shape of the material, given that the net magnetic dipoles depend on the shape of the outer boundaries of the sample (JOHNSON et al., 1996; PESSOA, 2010).

In general, the energy density is expressed as

$$\varepsilon_{dem} = -\frac{\mu_0}{2V}\int_{\text{sample volume}} dV\mathbf{M}\cdot\mathbf{H_{dem}}. \tag{2.4}$$

For a uniformly magnetized thin film with magnetization M_s, the energy density reads as

$$\varepsilon_{dem} = \frac{1}{2}\mu_0 M_s^2 cos^2\theta, \tag{2.5}$$

where θ is the angle with the film normal (WEI, 2015; JOHNSON et al., 1996). In this case, the demagnetizing anisotropy tends to align the magnetic moments parallel to the film plane (FARLE, 1998).

2.1.4 Magnetocrystalline anisotropy energy

In crystalline materials, the energy of the system depends on the orientation of the magnetization with respect to the crystallographic axes (PESSOA, 2010). The magnetocrystalline anisotropy is mostly caused by the spin-orbit interaction (JOHNSON et al., 1996).

For cubic systems, the cubic anisotropy energy is written as

$$\varepsilon_c = K_1\cdot\left(cos^2\alpha\cdot cos^2\beta + cos^2\beta\cdot cos^2\gamma + cos^2\gamma\cdot cos^2\alpha\right) + K_2\cdot cos^2\alpha\cdot cos^2\beta\cdot cos^2\gamma, \tag{2.6}$$

where K_1 and K_2 are the first and second order cubic anisotropy constants of the material and α, β and γ are the angles between the magnetization vector and the crystal axes (WEI, 2015).

And for systems with uniaxial symmetry,

$$\varepsilon_{uni} = K_u\cdot sin^2\alpha, \tag{2.7}$$

where K_u is the uniaxial anisotropy constant of the material and α is the angle between the magnetization and the easy axis (WEI, 2015).

Another common way to write the uniaxial anisotropy energy is $\varepsilon_{uni} = -K_u \cdot cos^2\alpha$ (ALAYO; XING; BAGGIO-SAITOVITCH, 2009). The two expressions differ only by a constant offset (K_u). This is essentially a gauge choice for the zero of energy, as the relevant physical quantity depends only on the variation of the energy with angle, which is minimal at 0 and 180 degrees in both cases.

2.1.5 Perpendicular anisotropy energy

The perpendicular anisotropy energy is significant in thin films and tends to align the magnetization perpendicular to the film plane. This effect arises from the broken symmetry at the film's extended surfaces, giving rise to surface anisotropy (WEI, 2015).

The energy density is given by

$$\varepsilon_{sur} = \frac{K_s}{t}, \tag{2.8}$$

where K_s is the surface anisotropy constant and t is the thickness of the layer (WEI, 2015).

In thin films, there is competition between perpendicular and demagnetizing anisotropy. The negative slope of Figure 6 indicates that, below a certain thickness, the interface anisotropy contribution outweighs the volume contribution, resulting in a perpendicularly magnetized system (JOHNSON et al., 1996).

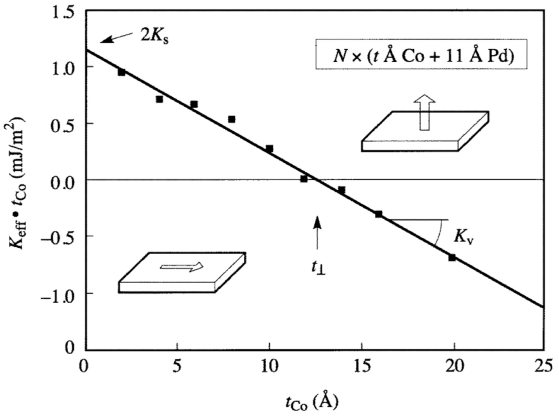

Figure 6 – Magnetic anisotropy energy per area versus the individual Co layer thickness of Co/Pd multilayers (JOHNSON et al., 1996).

2.1.6 Magnetoelastic anisotropy energy

Strain and lattice distortions cause changes in magnetocristallyne anisotropy, which may alter the direction of magnetization (JOHNSON et al., 1996; FARLE, 1998). In thin films, distortions may be induced by many factors, including thermal mismatch due to differences in thermal expansion coefficients, intrinsic strain introduced by the deposition process, and lattice mismatch between neighboring layers (PESSOA, 2010).

The energy density associated with this effect for an elastically isotropic medium can be written as

$$\varepsilon_{me} = -K_{me} \cdot cos^2\nu, \tag{2.9}$$

with

$$K_{me} = -\frac{3}{2}\lambda\sigma, \tag{2.10}$$

where ν is the angle between the magnetization and the direction of uniform stress, λ is the magnetostriction constant and σ is the stress (JOHNSON et al., 1996).

2.2 Magnetic coupling between layers

The exchange coupling of magnetic layers separated by a nonmagnetic metallic spacer causes, for small external fields, the layers' magnetization to align either ferromagnetically or antiferromagnetically. This interlayer exchange coupling was first observed in 1986 for dysprosium and gadolinium films separated by yttrium spacer (GRÜNBERG, 2001; BUSCHOW, 2005).

A phenomenological description of the magnetic coupling gives the interlayer coupling energy per unit area, E_i, as

$$E_i = -J_1\frac{\mathbf{M_A}\cdot\mathbf{M_B}}{M_A M_B} - J_2\left(\frac{\mathbf{M_A}\cdot\mathbf{M_B}}{M_A M_B}\right)^2, \tag{2.11}$$

where $\mathbf{M_A}$ and $\mathbf{M_B}$ are the magnetization vectors of the two FM layers. J_1 and J_2 are the bilinear and biquadratic coupling constants, respectively, both given in units of erg/cm^2. Alternatively, equation 2.11 can be written as

$$E_i = -J_1 cos(\theta) - J_2 cos^2(\theta), \tag{2.12}$$

with θ being the angle between the magnetizations of the FM films on both sides of the spacer layer. The parameters J_1 and J_2 determine both the type and strength of

the coupling. When J_1 is dominant, the coupling is collinear (ferromagnetic for $J_1 > 0$ and antiferromagnetic for $J_1 < 0$). In contrast, when J_2 is dominant and negative, the system favors a 90° coupling (WEI, 2015; BUSCHOW, 2005; ALAYO; XING; BAGGIO-SAITOVITCH, 2009).

The interlayer coupling is understood to result from the combined contributions of ferromagnetic pinhole coupling, magnetostatic Néel (orange-peel) coupling, and oscillatory coupling (ALAYO; BAGGIO-SAITOVITCH, 2010).

Bobo et al. (BOBO; FISCHER; PIECUCH, 1993) proposed an intrinsic coupling mechanism based on the presence of ferromagnetic coupling through pinholes (HEINRICH; COCHRAN, 1993). Pinholes are nanoscale gaps or defects in a thin film or at the interface between two magnetic layers that cause partial contact between the successive layers (BOBO; FISCHER; PIECUCH, 1993). Their effect in coupled layers is to create a direct ferromagnetic bridge between the layers. However, ferromagnetic coupling through pinholes should take place in samples with spacer thicknesses below 8 Åand is largely avoidable (ALAYO; XING; BAGGIO-SAITOVITCH, 2009; BUSCHOW, 2005).

Magnetostatic Néel coupling is caused by correlated roughness of interface between the FM layer and the spacer layer, which leads to free magnetic poles of opposite sign across the nonmagnetic layer that causes FM coupling (BUSCHOW, 2005; ALAYO; BAGGIO-SAITOVITCH, 2010). This so-called orange peel coupling decreases exponentially with spacer layer thickness. Furthermore, it is frequently observed in magnetic sandwiches and spin valves in particular (MORITZ et al., 2004).

Lastly, oscillatory or RKKY-like type of coupling favors a ferromagnetic or antiferromagnetic alignment between the FM layers depending on the thickness of the spacer layer and its strength decreases with the thickness (ALAYO; XING; BAGGIO-SAITOVITCH, 2009). Although these oscillations are similar to RKKY oscillations, their period is longer than that expected from the conventional RKKY framework (MATHON, 1991). This type of coupling arises from spin-dependent electron reflections at the interfaces of the nonmagnetic layer (ALAYO; BAGGIO-SAITOVITCH, 2010).

2.3 The exchange bias effect

Materials with a ferromagnetic(FM)/antiferromagnetic(AFM) interface exhibit an anisotropy induced in the FM. This exchange anisotropy is associated to the exchange bias phenomenon (EB), which was discovered in 1956 by Meiklejohn and Bean in Co particles (FM) coated with CoO (AFM) and presented itself as a shifted ferromagnetic hysteresis loop. Thus, the absolute value of the coercive field for decreasing and increasing external magnetic field is different (NOGUÉS; SCHULLER, 1999; COEY, 2010).

From an application standpoint, this phenomenon is of considerable significance in permanent magnets, magnetic recording media, domain stabilizers in recording heads, giant magnetoresistance systems, and spin valves. Most of the devices based on exchange bias properties are fabricated in thin film form, which is mostly due to the possibility of better control and characterization of the interface in bilayers (NOGUÉS; SCHULLER, 1999; COEY, 2010; KIWI, 2001).

An intuitive explanation of EB can be outlined by assuming an exchange interaction at the FM/AFM interface. When a magnetic field is applied in the temperature range $T_N < T < T_C$, the FM spins align with the field, while the AFM spins remain random. By cooling to $T < T_N$, the AFM spins next to the interface align ferromagnetically with those of the FM. When lowering and reversing the field, the FM spins start to rotate, while, for sufficiently large AFM anisotropy, the AFM spins remain unchanged. Thus, the AFM spins at the interface exert a torque on the FM spins to keep them in their original position. Therefore, it is created an unidirectional anisotropy at the FM spins and the field needed to reverse completely the FM layer is larger than it would be with no AFM layer. This causes the shift in the hysteresis loop (see Figure 7) (NOGUÉS; SCHULLER, 1999), which defines the exchange bias field (H_{ex}) as the distance from the center of the loop to the origin (COEY, 2010). In conclusion, exchange bias leads to a unidirectional anisotropy of the ferromagnetic layer, pinning its magnetization into a preferred direction (BUSCHOW, 2005).

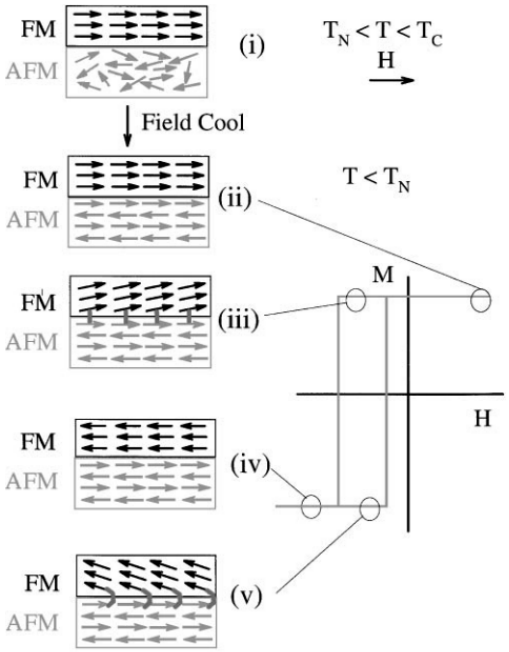

Figure 7 – Schematic diagram of the spin configuration of an FM-AFM bilayer at different stages of an exchange biased hysteresis loop (NOGUÉS; SCHULLER, 1999).

Although the exchange bias effect has been known for almost 70 years, new and

surprising phenomena continue to emerge, as well as novel materials exhibiting exchange bias under unexpected conditions (BLACHOWICZ; EHRMANN, 2021). There are several theoretical models that attempt to explain the exchange bias phenomenon in its many forms. Yet, no single theory has fit and described all the systems that exhibit EB (KIWI, 2001). Among the most debated aspects are the dependence of the exchange bias field on the thickness of both the ferromagnetic (FM) and antiferromagnetic (AFM) layers, as well as the influence of the magnetic structure of the AFM, particularly whether it is compensated or uncompensated. The orientation of the AFM spins also plays a crucial role, as does the degree of disorder at the FM/AFM interface. Additional factors include the magnetic anisotropy of the layers, the blocking temperature at which the exchange bias sets in, and the training effect, which refers to the gradual change in bias field upon repeated cycling of the hysteresis loop. Models also attempt to explain variations in coercivity, the impact of the applied cooling field, and the possibility of perpendicular coupling between FM and AFM spins. Collectively, these experimental features pose significant challenges and serve as criterion for the validity of proposed theoretical frameworks (NOGUÉS; SCHULLER, 1999).

Following the perspectives outlined by Kiwi and Blachowicz (KIWI, 2001; BLACHOWICZ; EHRMANN, 2021), the main models that seek to explain exchange bias will be presented and discussed in the following paragraphs.

One of the first attempts to develop a model to explain EB was made by Meiklejohn (MEIKLEJOHN, 1962). It was based on a single domain antiferromagnet in juxtaposition to a single domain ferromagnet with a plane interface, with the coupling at the interface being weaker than either the FM or the AFM. Coherent rotation of the FM and AFM was assumed as well as an uncompensated AFM interface (KIWI, 2001). The energy expression was written as

$$E = -HMcos\left(\theta - \beta\right) + K_{AFM}sin^2\alpha - J_Kcos\left(\beta - \alpha\right), \tag{2.13}$$

where E is the energy per unit volume of the ferromagnet, H is the applied magnetic field, M is the magnetic moment per unit volume of ferromagnet, K_{AFM} is the crystalline anisotropy energy per unit volume of AFM, J_K is the exchange anisotropy energy per unit volume of FM, and θ, β and α are the angles made by the applied field, the FM magnetization and the AFM anisotropy, respectively (MEIKLEJOHN, 1962). The value obtained for the exchange bias field H_{ex} is overestimated by orders of magnitude compared to that observed experimentally (KIWI, 2001; BLACHOWICZ; EHRMANN, 2021).

Other important contribution was made in 1967 by Néel (NÉEL, 1967). The model was based on collinear AFM and bulk FM magnetization, with a weakly anisotropic and uncompensated AFM interface. The magnetic moment direction is treated as a continu-

ous function of depth in the layer, and this continuum approximation plays a central role in the model. Néel found that domains can be created in the equilibrium state, predicted asymmetric hysteresis loops, discussed thermal treatment and magnetic history, and addressed interface disorder. However, the continuum approximation requires bulk ferromagnet, which compromises its application to thin films (KIWI, 2001; BLACHOWICZ; EHRMANN, 2021).

Following the first models, Malozemoff (MALOZEMOFF, 1987) proposed a model based on the presence of random interface roughness, as illustrated in Figure 8, which gives rise to a random field acting on the interface spins of FM-AFM sandwiches. Reasonable estimate values for the exchange bias field were obtained. Another model based on random interface was suggested by Schultess and Butler (SCHULTHESS; BUTLER, 1998; SCHULTHESS; BUTLER, 1999). They demonstrate that spin-flop coupling alone does not produce exchange bias and that exchange bias appears only when interface defects introduce local uncompensated moments, functionally equivalent to Malozemoff's random fields.

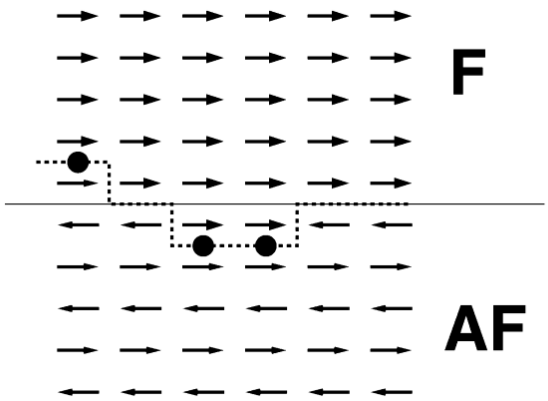

Figure 8 – AF rough interface with frustrated interactions marked by full dots (KIWI, 2001).

Models that include non-collinear orientations of FM and AFM spins (as shown in Figure 9), such as the ones presented by Mauri et al. (MAURI et al., 1987) and Morales et al. (MORALES et al., 2015), enable domain parallel to the interface. While Mauri locates the domain wall in the AFM and finds a limit to the exchange bias field, Morales locates the domain wall in the FM and shows non-uniform spin structure across the FM thickness, breaking the deviation from the inverse proportionality of the EB with the thickness of the FM layer.

The spin-glass-like models, initially introduced by Kiwi et al. (KIWI et al., 1999; KIWI et al., 2000; KIWI, 2001), interpret the interfacial region as a disordered magnetic phase with frozen, randomly oriented spins, drawing analogies with canonical spin-glass

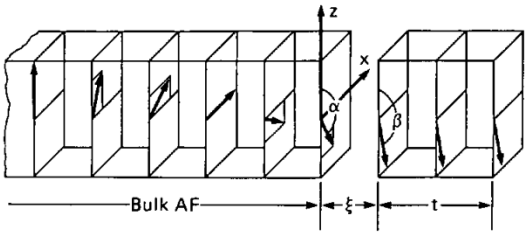

Figure 9 – Illustration of Mauri's model for the interface of a thin ferromagnetic film on a thick antiferromagnetic substrate. The spins of only one sublattice of the antiferromagnet are shown (MAURI et al., 1987)

.

systems. In Kiwi's model, the antiferromagnetic interface monolayer reconstructs into a rigid, canted magnetic structure that freezes into a metastable spin-glass-like configuration upon cooling. Later, Radu et al. (RADU et al., 2005) presented a modified Meiklejohn-Bean model with spin disorder. Also, O'Grady et al. (O'GRADY; FERNANDEZ-OUTON; VALLEJO-FERNANDEZ, 2010) suggested a grain-based model, in which each AF grain acts as a single domain, reversing independently, and disordered spins at the FM/AFM interface form clusters analogous to a spin glass, influencing coercivity and coupling.

Other grain-based models consider the exchange bias effect as arising from the collective behavior of multiple AFM grains, each potentially contributing differently to the overall bias depending on size, orientation, and coupling strength. Stiles and McMichael (STILES; MCMICHAEL, 1999) model the antiferromagnet as independent grains that are coupled to a ferromagnetic film both by direct coupling to the net moments at the interfaces of the grains and by spin-flop coupling. Saha and Victoria (SAHA; VICTORA, 2006) proposed a micromagnetic simulation-based model in which the FM interface grains were coupled to neighboring AFM grains that rotated uniformly under the effect of thermal fluctuations. Choo et al. (CHOO et al., 2007) used a granular Monte Carlo approach for the AFM layer as the AFM state was assumed to be dominated by thermal processes. And Harres and Geshev (HARRES; GESHEV, 2012) explicitly models the FM/AFM interface as an ensemble of grains, where each grain is classified as either stable (contributes to unidirectional anisotropy) or unstable (enhances coercivity).

Finally, in the context of core–shell nanoparticles, models like the ones introduced by Iglesias et al. (IGLESIAS; LABARTA; BATLLE, 2008) and Dimitriadis et al. (DIMITRIADIS et al., 2015) focus on the magnetic interaction between a ferromagnetic core and an antiferromagnetic or shell. Both apply the Heisenberg model with uniaxial anisotropy using a Monte Carlo simulation.

3 Ferromagnetic resonance in magnetic thin films

Magnetic resonance spectroscopy is a group of techniques, involving the interaction between an electromagnetic field and a substance, that provides information on the magnetic properties of matter. Depending on the origin of the magnetic property investigated (electronic, nuclear or from collective excitations), the technique may be Electron Paramagnetic Resonance (EPR), Nuclear Magnetic Resonance (NMR) or Ferromagnetic Resonance (FMR) (YALÇIN, 2013; SOVSKII, 2016).

Ferromagnetic resonance is a powerful tool for investigating the magnetic properties of ferromagnetic materials. It can be applied to nanosystems (YALÇIN, 2013) and, for thin films in particular, the FMR technique enables the measurement of all key parameters that characterize magnetic properties, including magnetic anisotropy, g-value, magnetic moment, Curie temperature, magnetoelastic coupling coefficients, and magnetization relaxation mechanisms. Moreover, FMR has the advantages of being a high-sensitivity and high-resolution technique, that measures ground-state properties and can provide information on the magnetic and structural quality of a thin film (FARLE, 1998; LINDNER; BABERSCHKE, 2003). This chapter introduces the theoretical foundations of FMR, outlining the main mathematical approaches used to describe the resonance condition.

3.1 Ferromagnetic Resonance

When a ferromagnet is exposed to a uniform magnetic field $\mathbf{H_0}$ and a transverse high-frequency field from microwave radiation, the resonance phenomenon may be observed (COEY, 2010). Resonance occurs when the frequency of the microwave field is equal to the precession frequency of the magnetization (GUIMARÃES; OLIVEIRA, 1998). Experimentally, the frequency of the microwave field is kept constant and the intensity of the external field is varied. The resonant absorption of microwave energy by the material is detected (SOVSKII, 2016). In contrast, in cavity-free FMR configurations, the resonance condition can be accessed by varying the microwave frequency, as the system is no longer constrained by the fixed frequency of a resonant cavity (SCHMOOL et al., 2021).

The system can be treated classically, like a giant spin, or macrospin. In essence, the magnetization of the sample is assumed to be uniform. (COEY, 2010). The magnetization vector $\mathbf{M}$ will tend to align with the effective magnetic field H_{eff}, in order to minimize the energy of the system. On the other hand, the microwave magnetic field $\mathbf{h}$ will apply a torque on the magnetic moment, triggering a precessional motion of the magnetization

around the external magnetic field (WEI, 2015). The motion for the magnetization, in the absence of damping, is described by the Laundau-Lifshitz equation:

$$\frac{d\mathbf{M}}{dt} = -\gamma \mathbf{M} \times \mathbf{H_{eff}}. \tag{3.1}$$

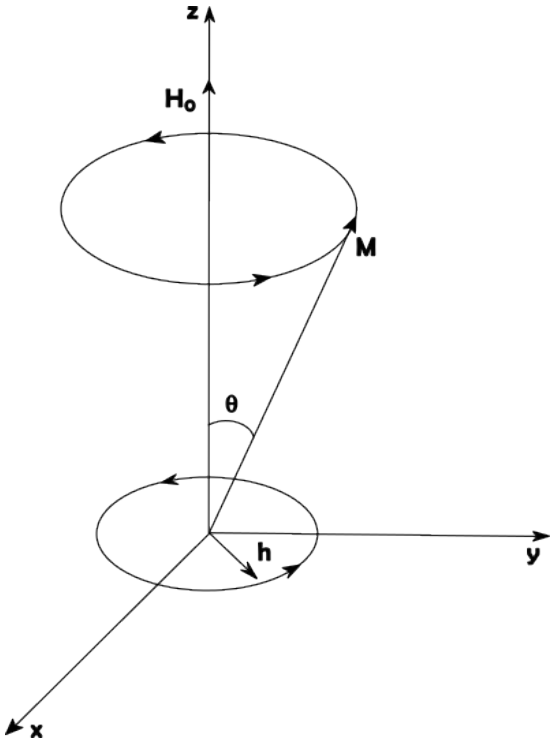

Figure 10 – Precession of the magnetization vector **M** in a static magnetic field $\mathbf{H_0}$ and a microwave magnetic field **h** (SOVSKII, 2016).

The effective field must be distinguished from the external field $H = B/\mu_0$. The former is present inside the ferromagnet, that is $H_{eff} = H + H_d$. The demagnetizing field $H_d = -\mathcal{N}M$, where $\mathcal{N}$ is the demagnetizing tensor, which depends on the geometry of the sample (COEY, 2010). Therefore, the FMR measurement is influenced by the geometry of the sample (YALÇIN, 2013).

3.1.1 Smith-Suhl-Beljers approach

To evaluate the resonance condition, the system's natural frequency under a specific external field must be obtained by solving the equation 3.1. However, finding a general analytical solution is generally impractical (WEI, 2015). In 1955, Smit, Suhl and Beljers (SUHL, 1955; SMIT; BELJERS, 1955) obtained the resonance condition for a ferromagnet in terms of the total free energy density. Its main limitation is that it provides only the resonance fields, without direct access to other spectral features. In spite of this limitation, the approach is particularly well suited for the study of thin films. The intensities

and linewidths of the resonance signals can be deduced using the Landau-Lifshitz formalism (LINDNER; BABERSCHKE, 2003). We now derive the Smit-Shul-Beljers resonance condition following the procedure described in (WEI, 2015), with some modifications to suit the current context.

From the Laundau-Lifshtz equation,

$$\begin{aligned}\frac{d\mathbf{M}}{dt} &= -\gamma \mathbf{M} \times \mathbf{H_{eff}} \\ &= -\gamma \left(M_s \hat{r}\right) \times \left(H_r \hat{r} + H_\theta \hat{\theta} + H_\phi \hat{\phi}\right)\end{aligned} \tag{3.2}$$

The total free energy density ε is given by

$$\varepsilon = -\mathbf{M} \cdot \mathbf{H_{eff}} = -\left(M_s \hat{r}\right) \cdot \left(H_r \hat{r} + H_\theta \hat{\theta} + H_\phi \hat{\phi}\right). \tag{3.3}$$

If $\mathbf{M}$ rotates by a small angle $\Delta\theta$,

$$\varepsilon' = -\left(M_s(\hat{r} + \Delta\theta_M \hat{\theta})\right) \cdot \left(H_r \hat{r} + H_\theta \hat{\theta} + H_\phi \hat{\phi}\right) \tag{3.4}$$

$$\Delta\varepsilon = \varepsilon' - \varepsilon = -M_s H_\theta \Delta\theta_M \tag{3.5}$$

$$\frac{\partial \varepsilon}{\partial \theta_M} = -M_s H_\theta \tag{3.6}$$

If $\mathbf{M}$ rotates by a small angle $\Delta\phi$,

$$\varepsilon'' = -\left(M_s(\hat{r} + \Delta\phi_M sin\theta_M \hat{\phi})\right) \cdot \left(H_r \hat{r} + H_\theta \hat{\theta} + H_\phi \hat{\phi}\right) \tag{3.7}$$

$$\Delta\varepsilon = \varepsilon'' - \varepsilon = -M_s sin\theta_M H_\phi \Delta\phi_M \tag{3.8}$$

$$\frac{\partial \varepsilon}{\partial \phi_M} = -M_s sin\theta_M H_\phi \tag{3.9}$$

By substituting 3.6 and 3.9 into 5.3,

$$\begin{cases} \frac{dM_s}{dt} & = 0 \\ -\frac{M_s}{\gamma} sin\theta_M \frac{d\theta_M}{dt} & = \frac{\partial \varepsilon}{\partial \phi_M} \\ \frac{M_s}{\gamma} sin\phi_M \frac{d\theta_M}{dt} & = \frac{\partial \varepsilon}{\partial \theta_M} \end{cases} \tag{3.10}$$

The system of equations above can be solved by rewriting it in terms of the equilibrium angle values, $\theta_{M,equi}$ and $\phi_{M,equi}$, and their small deviations $\delta\theta_M$ and $\delta\phi_M$. That is,

$$\begin{aligned} \theta_M &= \theta_{M,equi} + \delta\theta_M \\ \phi_M &= \phi_{M,equi} + \delta\phi_M. \end{aligned} \tag{3.11}$$

This equilibrium position, where the system's energy density is at its minimum, can be determined by

$$\begin{aligned} \frac{\partial \varepsilon}{\partial \theta_M} &= 0 \\ \frac{\partial \varepsilon}{\partial \phi_M} &= 0. \end{aligned} \tag{3.12}$$

The derivatives $\frac{\partial \varepsilon}{\partial \theta_M}$ and $\frac{\partial \varepsilon}{\partial \phi_M}$ can also be rewritten by a Taylor series expansion up to linear terms:

$$\begin{aligned} \frac{\partial \varepsilon}{\partial \theta_M} &= \frac{\partial^2 \varepsilon}{\partial \theta_M^2}\delta\theta_M + \frac{\partial^2 \varepsilon}{\partial \theta_M \partial \phi_M}\delta\phi_M \\ \frac{\partial \varepsilon}{\partial \phi_M} &= \frac{\partial^2 \varepsilon}{\partial \phi_M \partial \theta_M}\delta\theta_M + \frac{\partial^2 \varepsilon}{\partial \phi_M^2}\delta\phi_M \end{aligned} \tag{3.13}$$

Substituting 3.11 and 3.13 into the second and third equations of 3.10, we get

$$\begin{cases} -\frac{M_s}{\gamma} sin\theta_M \frac{d\delta\theta_M}{dt} &= \frac{\partial^2 \varepsilon}{\partial \phi_M \partial \theta_M}\delta\theta_M + \frac{\partial^2 \varepsilon}{\partial \phi_M^2}\delta\phi_M \\ \frac{M_s}{\gamma} sin\phi_M \frac{d\delta\theta_M}{dt} &= \frac{\partial^2 \varepsilon}{\partial \theta_M^2}\delta\theta_M + \frac{\partial^2 \varepsilon}{\partial \theta_M \partial \phi_M}\delta\phi_M \end{cases} \tag{3.14}$$

The equations above will have a periodic solution $\delta\theta_M$, $\delta\phi_M \sim e^{i\omega t}$, with ω being the frequency of the microwave magnetic field. Therefore 3.10 can be written, in the matrix form, as the following:

$$\begin{pmatrix} \left(\frac{\partial^2 \varepsilon}{\partial \phi_M \partial \theta_M} + \frac{M_s}{\gamma} sin\theta_M i\omega\right) & \frac{\partial^2 \varepsilon}{\partial \phi_M^2} \\ \frac{\partial^2 \varepsilon}{\partial \theta_M^2} & \left(\frac{\partial^2 \varepsilon}{\partial \theta_M \partial \phi_M} - \frac{M_s}{\gamma} sin\theta_M i\omega\right) \end{pmatrix} \times \begin{pmatrix} \delta\theta_M \\ \delta\phi_M \end{pmatrix} = \begin{pmatrix} 0 \\ 0 \end{pmatrix} \tag{3.15}$$

Given that the determinant of the coefficient matrix must be zero for the system to have nontrivial solutions, we arrive at the equation for the resonance condition

$$\left(\frac{\omega_{res}}{\gamma}\right)^2 = \frac{1}{M_s^2 sin^2\theta_M}\left[\frac{\partial^2 \varepsilon}{\partial \theta_M^2}\frac{\partial^2 \varepsilon}{\partial \phi_M^2} - \left(\frac{\partial^2 \varepsilon}{\partial \theta_M \partial \phi_M}\right)^2\right]_{\theta_M=\theta_{M,equi},\phi_M=\phi_{M,equi}}. \tag{3.16}$$

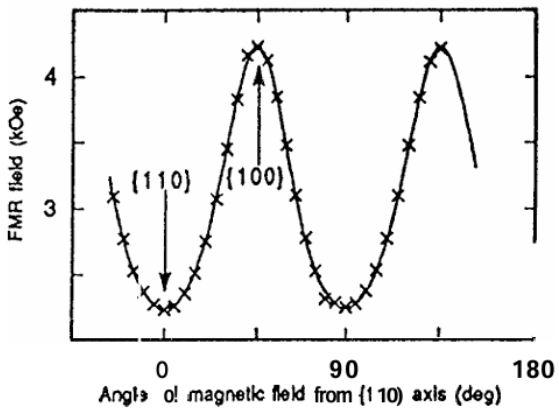

Figure 11 – In-plane angular dependence of the resonance field observed for $(Co)_{4\,3}/(Cu)_6/(Co)_4$ film. From (WIGEN; ZHANG, 1992).

The resonance condition is strongly influenced by the magnetic anisotropies and symmetries present in the sample, which determine the equilibrium positions. As a result, an analysis of the angular dependence of the FMR resonance field provides a means of both identifying and quantifying the symmetry of these anisotropy contributions. For example, as illustrated in Figure 11, a sample exhibiting cubic magnetocrystalline anisotropy displays a characteristic fourfold symmetry in the in-plane angular dependence of the resonance field.

Parte II

Experimental procedures

4 Si/Ru/IrMn/Co/Ru(x)/Py/IrMn/Ru multilayers

This chapter describes the primary experimental procedures employed in the synthesis, structural characterization of the multilayers and magnetic measurement techniques used to investigate the system, focusing on ferromagnetic resonance (FMR) and complementary magnetization measurements.

4.1 Deposition by Magnetron Sputtering

Magnetron sputtering is a physical vapor deposition technique in which an ionized gas (plasma) is used to eject atoms from a target and deposit them onto a substrate. In its simplest configuration, a DC-powered diode setup, a low-pressure glow discharge plasma forms between two planar electrodes. The substrate acts as the anode, while the cathode holds the target material. Energetic argon ions generated in the plasma bombard the target surface, ejecting atoms through a process known as sputtering. These atoms then travel through the chamber and condense onto the substrate, forming a thin film (KELLY; ARNELL, 2000; BRÄUER et al., 2010).

The multilayers systems Si/Ru(150Å)/IrMn(150Å)/Co(50Å)/Ru(tRu)/Py(50Å)/ /IrMn(150Å)Ru(50Å), where Py is the Ni80Fe20 alloy and IrMn is the Ir20Mn80 alloy were prepared by the Magnetron Sputtering technique. The thickness of the Ru layer (tRu) was varied between 8Åand 60Å, with tRu = 8, 10, 12, 14, 16, 18, 20, 22, 24, 26, 28, 32, 36, 40, 44, 48, 50, 55, 60Å. The Si(100) substract is monocristallyne and a Ru buffer layer was deposited subsequent to it. Another Ru layer was also deposited on top of the final IrMn layer to prevent oxidation, as illustrated in Figure 12.

The system used, equipped with DC and RF sources, enables the preparation of multilayers of metals (magnetic or non-magnetic), alloys, and oxides. It operates with a base pressure of 10^{-8} Torr and receives Ar gas at a pressure of 10^{-3} Torr for plasma production. It is composed of two cylindrical chambers. The main chamber houses five magnetron sources, each equipped with a gas ring, shield chimneys, and pneumatic shutters. Targets are mounted on the magnetrons, which are powered by DC, RF, or pulsed DC supplies, depending on the material. Up to five substrate holders can be placed inside the chamber on a rotating base, which also features a heater stage capable of controlling substrate temperatures from 25 to 1000 ^oC. The second chamber, with diameter of 100 mm, is connected to the main chamber through a manual ultra-high vacuum valve. This configuration enables substrate holders to be inserted or removed without breaking the

vacuum of the main chamber.

The deposition was made with an applied magnetic field produced by two NdFeB magnets attached to the sample holder, the base pressure used varied from approximately 2×10^{-8} Torr to 6×10^{-8} Torr and the argonium working pressure was 8×10^{-3} Torr for the IrMn layers and 3×10^{-3} Torr for the other layers. The samples were grown by Dr. Isabel Liz Castro and Dr. Liying Liu at Centro Brasileiro de Pesquisas Físicas (CBPF).

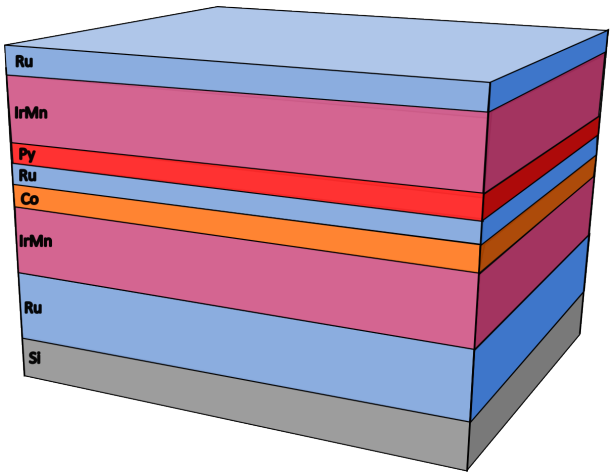

Figure 12 – Illustration representing the Si/Ru/IrMn/Co/Ru(x)/Py/IrMn/Ru multilayers.

4.2 Structural characterization

Grazing-Incidence X-ray Diffraction (GIXD) was used to calculate the thickness and deposition rate of the layers and the structural character of each layer was determined by Conventional X-ray Diffraction (XRD). Crystal structure, texture, surface roughness and identification of the phases present in the samples were obtained rom the analysis of these measurements.

Additional analyses of the samples' morphology and chemical composition were obtained from measurements performed using Transmission Electron Microscopy (TEM), Scanning Electron Microscopy (SEM), and Scanning Transmission Electron Microscopy (STEM). The latter equipment is installed at the Institute of Physics, at LABNANO, and at the High-Resolution Electron Microscopy Laboratory (Laboratório de Microscopia Eletrônica de Alta Resolução - LaMAR) at UFF. All structural characterizations were performed by Dr. Isabel Liz Castro and Dr. Liying Liu at CBPF.

4.3 FMR experimental setup and measurements

A basic spectrometer consists of three essential components: a source of electromagnetic radiation, a sample, and a detector. In the Bruker EPR system, the source and detector are integrated in the microwave bridge, the sample is placed inside a microwave cavity (or resonator), and the console contains the electronics for signal processing and control. In addition, a computer coordinates all the modules and performs data acquisition and analysis. A scheme of the equipment components is presented in Figure 13 (WEBER, 2011).

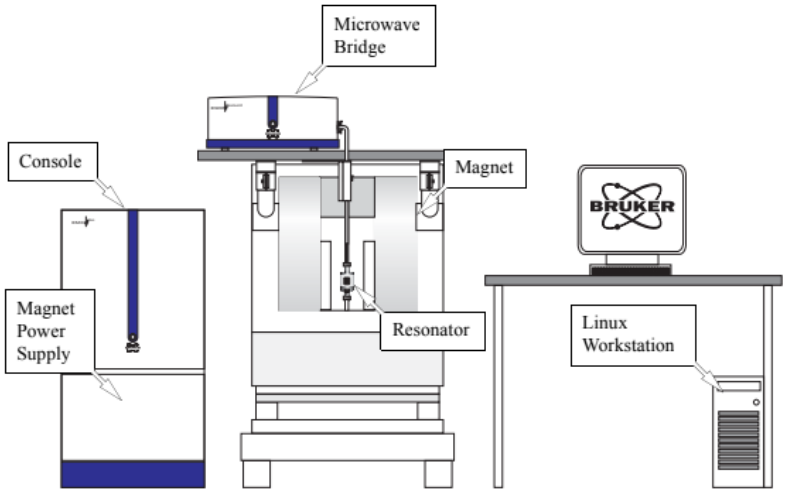

Figure 13 – Schematic representation of the modules and components of the EMXplus spectrometer (WEBER, 2011).

The microwave cavity, typically a rectangular or cylindrical metal box, is used to amplify weak signals from the sample by resonating with the microwaves. At resonance, microwaves remain confined within the cavity instead of being reflected, giving rise to standing waves. In this regime, the electric and magnetic fields are spatially separated and out of phase. By placing the sample at the position of maximum magnetic field and minimum electric field, the spectrometer achieves maximum signal strength and sensitivity.

All of these properties of a cavity give rise to a signal by the absorption of microwave by the sample. When that happens, the cavity is therefore no longer critically coupled and microwave will be reflected back to the bridge, resulting in a signal. To further enhance sensitivity, the spectrometer uses phase-sensitive detection, implemented in the console's signal channel. This technique reduces noise and suppresses baseline instabilities, transforming the response into a sine wave (the first derivative of the absorption curve) whose amplitude is proportional to the slope of the signal.

Finally, the spectrum is represented by the first derivative of an absorption line, as presented in Figure 14. Its main parameters are the peak-to-peak amplitude, the peak-

to-peak linewidth, linked to microscopic magnetization relaxation mechanisms, and the resonance field, corresponding to the static magnetic field at which resonance occurs.

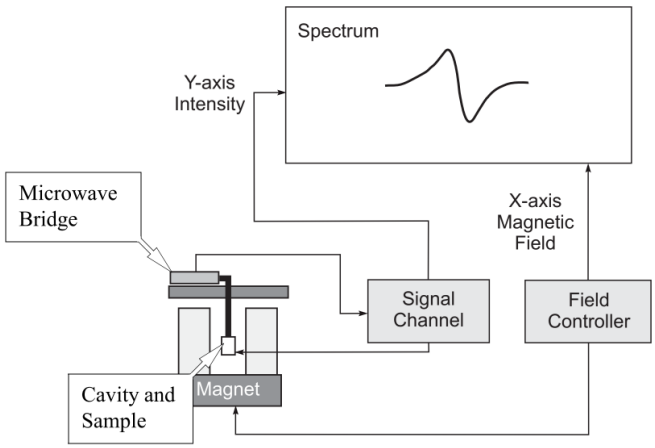

Figure 14 – Block diagram of an EPR spectrometer. (WEBER, 2011).

FMR experiments were performed at Paramagnetic Resonance laboratory, at UnB, using a Bruker EMXplus (Bruker, Germany). The spectrometer is equipped with an X-band microwave bridge and a high-sensitivity resonator (Bruker ER 4119HS, Germany). Measurements were made at room temperature, the sweep width was 4000 G, field modulation was applied at a frequency of 100 kHz with a modulation amplitude of 10 G. The microwave power was set to 2 mW.

Each sample was placed in the center of the rectangular resonant cavity attached to a goniometer, as shown in Figure 15. For each sample, spectra were acquired for various orientations of the sample with respect to the static magnetic field, with $0,1^0$ precision.

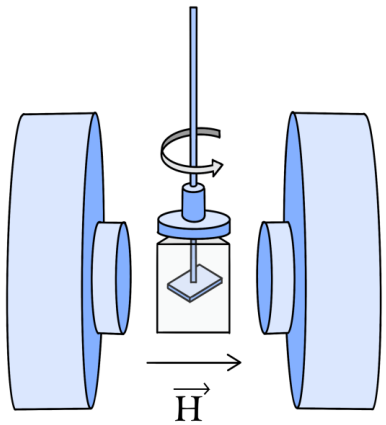

Figure 15 – Representation of sample placement in the cavity.

4.4 Magnetization measuremens

The vibrating sample magnetometer (VSM) technique is a magnetometry method sensitive to the static magnetization. It vibrates a sample sinusoidally up and down, which induces an electrical signal in a stationary pick-up coil. The signal is proportional to the magnetic moment, as well as to the amplitude and frequency of the vibration (BLUNDELL, 2001; LINDNER; BABERSCHKE, 2003).

Magnetization measurements as a function of the in-plane applied field were performed. Transitions were observed between –500 Oe and +500 Oe for Ru thicknesses ranging from 20 to 60 Å. For lower thicknesses, they may occur between -2000 Oe and +2000 Oe. Around the transition points, the field sweep step was reduced to increase resolution.

Magnetization measurements were carried out using the fully cryogen-free Dynacool and Versalab systems from Quantum Design, installed at the Interinstitutional Laboratory for Magnetic and Transport Measurements at CBPF with support from FAPERJ by Dr. Isabel Liz Castro and Dr. Liying Liu.

Parte III

Results and discussion

5 Results and discussion

Magnetic anisotropy constants can be indirectly determined from FMR measurements by fitting the experimental data to phenomenological models. In the FMR spectra, the lowest resonance field occurs when the external magnetic field is applied along the easy axis of magnetization, providing a straightforward means of identifying the anisotropy axes of the sample. By probing the angular dependence of the resonance field, it is possible to analyze information about the nature and strength of different anisotropy contributions, as well as the presence of exchange bias effects (PESSOA, 2010; FARLE, 1998; SOUSA, 2013). This chapter discusses the FMR measurements of the multilayers and these anisotropy contributions, including the exchange bias effect, that were acquired from the experimental data. The analysis method is addressed, and the behavior of the exchange bias field in the different samples is described.

5.1 FMR measurements

One of the FMR spectra obtained for the Ru 26 Å sample is presented in Figure 16. This representative spectrum accurately reflects the behavior observed across the entire sample set. There are two well defined transitions, which were attributed to the Co and Py layers resonance modes, respectively, as discussed in ALAYO et al., 2011 (ALAYO et al., 2011). Due to the fact that Co has greater saturation magnetization ($4\pi M_{Co} = 17$kOe) than Py ($4\pi M_{Py} = 10$kOe), its resonance occurs at lower fields.

The complete set of spectra from all angular orientations for the Ru 26 Å sample is presented in Figure 17. It is visible that the resonance fields of both transitions vary with the angular position. The spectra were fitted with combinations of first-derivatives of Lorentzian curves in order to determine the resonance fields (H_{res}) of each resonant mode. Figure 18 shows the variation of these resonance fields with the angular position, as well as an illustration representing the relative orientation of the external magnetic field with respect to the unidirectional anisotropy. The bell-shaped curve is a telling characteristic of the exchange bias effect, which is consistent with the unidirectional anisotropy induced by it (GLOANEC et al., 2010; SOUSA, 2013).

5.1.1 Energy model description for Smit-Beljers approach

The multilayer Si/Ru/IrMn/Co/Ru/Py/IrMn/Ru consists of two ferromagnetic layers (Co and Py). Each ferromagnet is adjacent to an antiferromagnetic IrMn layer, and the two are separated by a non-magnetic Ru spacer. Following the approach adopted

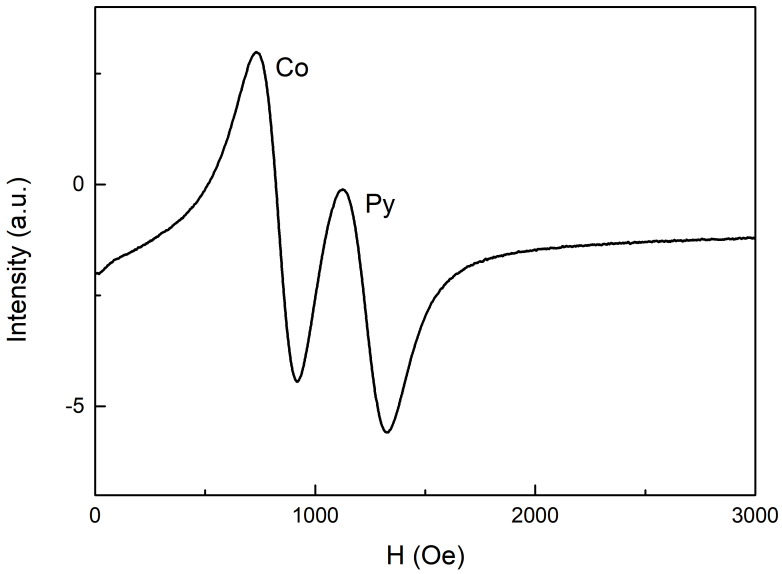

Figure 16 – FMR spectrum Ru 26 Åwith field parallel to the film plane.

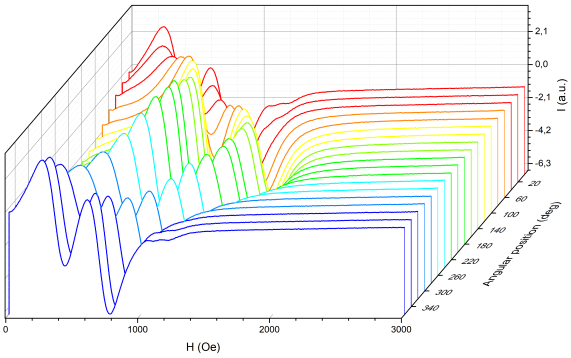

Figure 17 – FMR spectra for Ru 26 Å

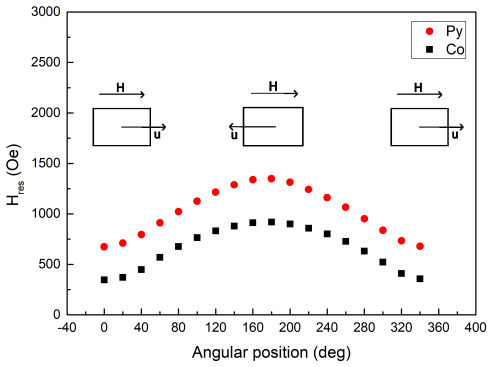

Figure 18 – H_{res} for Ru 26 Å

by GESHEV et al. (2001) and ALAYO et al. (2009) (GESHEV; PEREIRA; SCHMIDT, 2001; ALAYO; XING; BAGGIO-SAITOVITCH, 2009), the total energy density of such a multilayer can be written in the general form

$$\varepsilon = \varepsilon_{fm1} + \varepsilon_{fm2} + \varepsilon_{eb1} + \varepsilon_{eb2} + \varepsilon_{int}, \tag{5.1}$$

where ε_{fm_i}, $i = \{1, 2\}$ represents the energy density of the i^{th} ferromagnetic layer; ε_{eb_i}, $i = \{1, 2\}$ is the exchange bias interaction between the i^{th} FM layer and its adjacent AFM layer; and ε_{int} accounts for the magnetic interaction between the two FM layers.

If disregarded the magnetic interaction between the FM layers, each layer (and, consequently, each FMR resonant mode) can be modeled with the energy density that

follows:

$$\varepsilon_i = \varepsilon_{fmi} + \varepsilon_{ebi}, \tag{5.2}$$

with

$$\begin{aligned} \varepsilon_{fm_i} &= \varepsilon_{zee} + \varepsilon_{dem} + \varepsilon_{uni} \\ &= t_i \cdot \left[-\mathbf{H} \cdot \mathbf{M_i} + 2\pi(\mathbf{M_i} \cdot \mathbf{n})^2 - k_{u_i} \left(\frac{\mathbf{M_i} \cdot \mathbf{u}}{M_i} \right) \right] \end{aligned} \tag{5.3}$$

and, considering only contributions depending on the direction of the FMR layer's magnetization vector,

$$\varepsilon_{ebi} = J_{ebi} \frac{\mathbf{M_{afmi}} \cdot \mathbf{M_i}}{M_{afmi} \cdot M_i}, \tag{5.4}$$

where t_i, $\mathbf{M_i}$ and k_{u_i} are the thickness, saturation magnetization, and uniaxial anisotropy constant of the i^{th} FM layer, $\mathbf{n}$ is the unitary vector perpendicular to the film plane, J_{ebi} is the exchange bias constant between the i^{th} FM layer and its adjacent AFM layer and $\mathbf{M_{afmi}}$ is the saturation magnetization of this adjacent AFM layer.

In the coordinate system shown in Figure 19, the easy magnetization axes of the FM and AFM layers are aligned. Under this setup, both $\mathbf{H}$ and $\mathbf{M_{afmi}}$ lie in the film plane. With the effective fields introduced in equations 5.5 and 5.6, the energy density of the i^{th} FM layer can therefore be expressed as given in equation 5.7.

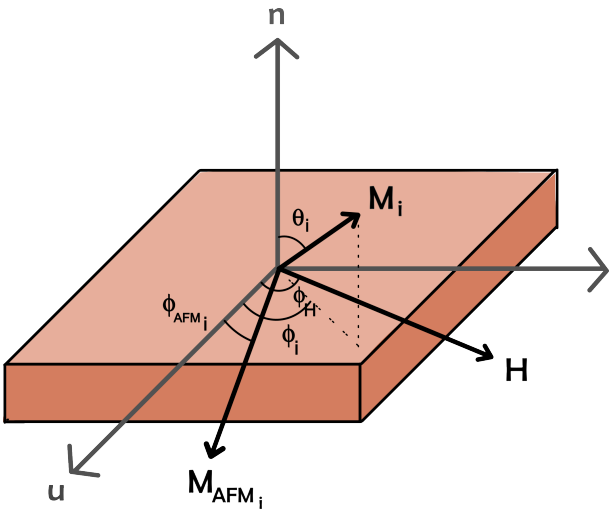

Figure 19 – Coordinate system for a single layer.

$$H_{ui} = \frac{2K_{ui}}{M_i} \tag{5.5}$$

$$H_{ebi} = \frac{J_{ebi}}{t_i M_i} \tag{5.6}$$

$$\begin{aligned} \frac{\varepsilon_i}{t_i} &= M_i \cdot [-Hsin\theta_i cos(\phi_H - \phi_i) + 2\pi M_i^2 cos^2\theta_i + \\ &- \frac{1}{2} H_{ui} sin^2\theta_i cos^2\phi_i - H_{ebi} sin\theta_i cos(\phi_i - \phi_{afmi})] \end{aligned} \tag{5.7}$$

5.1.2 Resonance field simulations

Simulations of the in-plane angular dependence of the resonance field were made by employing the single-layer Smit-Suhl-Beljers approach to determine the resonance condition. The method assumes uniform (saturated) magnetization and gives the resonance fields H_{res} for each angular position of the external field **H** by solving equations 3.12 and 3.16 with the energy density given by equation 5.7. In this last one, ϕ_{afmi} was chosen to be zero because it is known that, to achieve the unidirectional anisotropy caused by exchange bias and seen in the shape of the angular dependence of H_{res}, the magnetization of the AFM layer should remain fixed close to the easy axis, which minimizes the energy density (FARLE, 1998).

Equations 3.12 and 3.16 are coupled because every ϕ_H determines a new equilibrium position (ϕ_i, θ_i). Consequently, solving these equations is only possible by numerical calculations. The detailed calculations and Maple coding used to determine the resonance condition and the H_{res} X deg simulations are outlined in Appendix A.

The simulations and experimental data for the Py and the Co transitions for the Ru 16, 26, 40 and 60 Å samples are presented in Figures 20 to 27. From these theoretical simulations the effective magnetization, the uniaxial anisotropy field H_u, the exchange bias field H_{eb}, and the g-factor were obtained for all studied samples. The Pearson's correlation coefficients for each fit are reported in Tables 5.1.2 and 5.1.2. These coefficients confirm the adequacy of the simulations with the experimental data. The magnetization and effective uniaxial anisotropy values determined by fitting both transitions for all samples are presented in Table 3. These are suitable values for Py and Co thin films (ALAYO et al., 2011; SOUSA, 2013; BRIGNETI et al., 2008). It is observed that there is a slight asymmetry between the field coordinates of the first and last data points on some curves. This asymmetry can be attributed to the training effect, caused by repeated field cycling, which causes successive changes in uncompensated interfacial AFM magnetization (SOUSA, 2013).

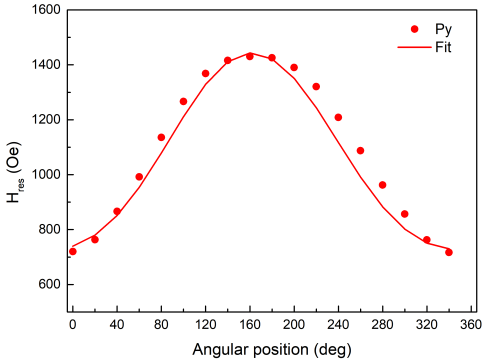

Figure 20 – Simulation Py - Ru 16 Å

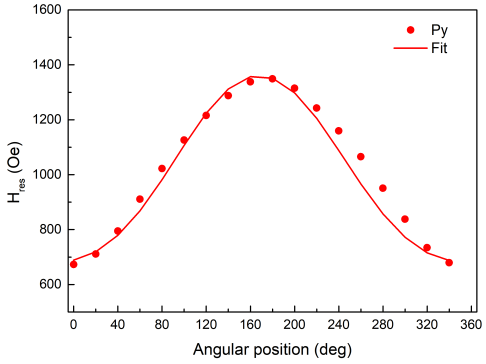

Figure 21 – Simulation Py - Ru 26 Å

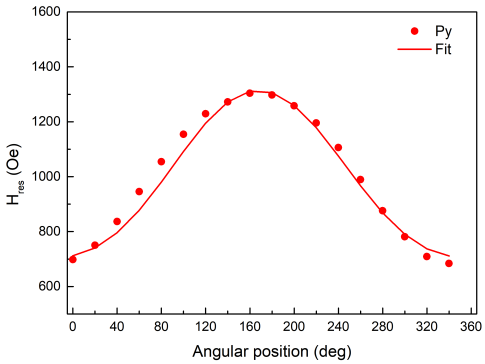

Figure 22 – Simulation Py - Ru 40 Å

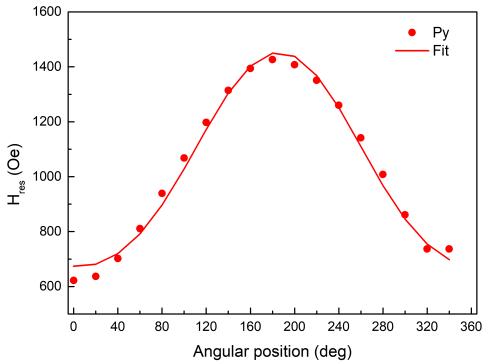

Figure 23 – Simulation Py - Ru 60 Å

t (Å)	8	10	12	14	16	18	22	24	26	40	44	48	50	55	60
r	0,97	0,99	0,99	0,99	0,98	0,99	0,99	0,99	0,98	0,99	0,99	0,90	0,95	0,98	0,99

Table 1 – Correlation coefficient for simulation and experimental data for Py.

5.1.3 Exchance bias field

The values of H_{eb} given by the simulation parameters are presented in Figures 28 and 29 for Py and Co transitions. The results indicate a non-monotonic and somewhat constant dependence of the exchange bias on the Ru(x) spacer thickness. The fluctuations observed in the exchange bias fields for both Py/IrMn and Co/IrMn interfaces are of the order of ±50 Oe.

The H_{eb} values for the IrMn/Py interface may be regarded as having an oscillatory-like behavior with the Ru layer thickness, specially for thinner layers. The data points oscillate around 340 Oe. Periodic changes in the exchange bias field may reflect the oscillatory RKKY interlayer exchange coupling between the Py and the Co layer through the Ru spacer, similar to the behavior discussed by POLISHCHUK et al., 2023 (POLISHCHUK

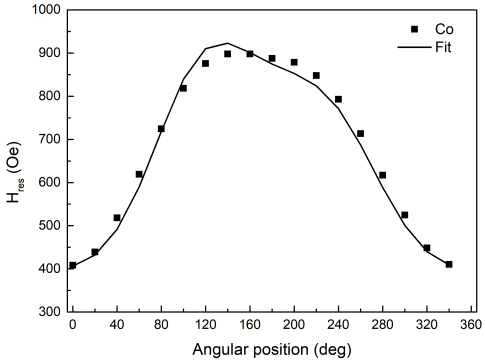

Figure 24 – Simulation Co - Ru 16 Å

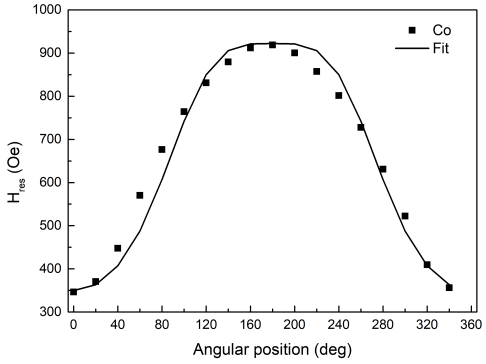

Figure 25 – Simulation Co - Ru 26 Å

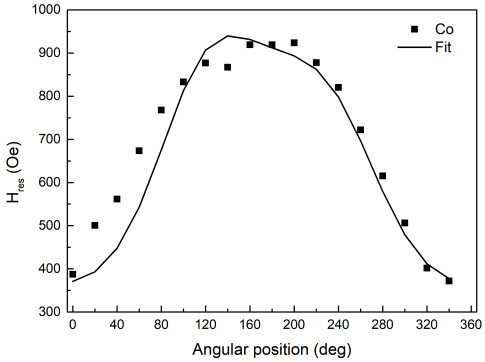

Figure 26 – Simulation Co - Ru 40 Å

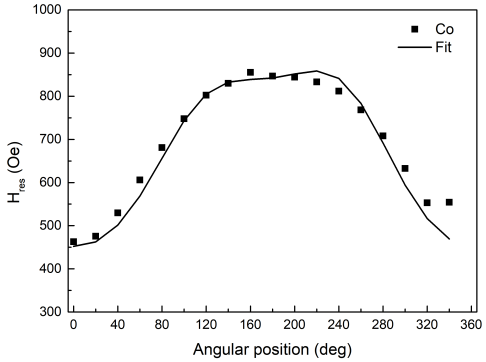

Figure 27 – Simulation Co - Ru 60 Å

t (Å)	8	10	12	14	16	18	22	24	26	40	44	48	50	55	60
r	-	0,98	-	0,81	0,99	0,99	0,99	0,97	0,98	0,97	0,98	0,90	0,93	0,94	0,99

Table 2 – Correlation coefficient for simulation and experimental data for Co.

et al., 2023).

The value for H_{eb} due to the IrMn/Co interface presented by ALAYO et al., 2010 (ALAYO; BAGGIO-SAITOVITCH, 2010), around 290 Oe for the same thickness of the IrMn and Co layers, is in agreement with some of the values found for the Py resonant mode, which fluctuate around 220 Oe with no sign of clear oscillatory behavior.

In both interfaces, fluctuations in H_{eb} can also be caused by grain size distribution in the AFM layers, interface roughness and interdiffusion, which are microscopic inhomogeneities favored by the sputtering technique. AFM grain size distribution leads to a distribution of pinning strengths between the FM and AFM layers and, therefore, a range of effective H_{eb} values (ZHANG; DRESSEL, 2009; MERKEL et al., 2022; SCHOLL et al., 2004). Slight variations in interface sharpness or chemical mixing, such as roughness

	M (emu/cm^3)	H_u (Oe)
Py	800	5
Co	1400	60

Table 3 – Magnetization and effective uniaxial anisotropy field for Py and Co .

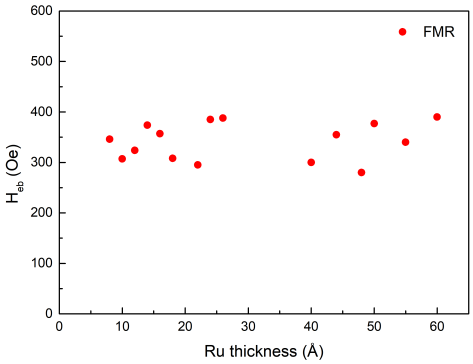

Figure 28 – H_{eb} Vs Ru thickness for Py.

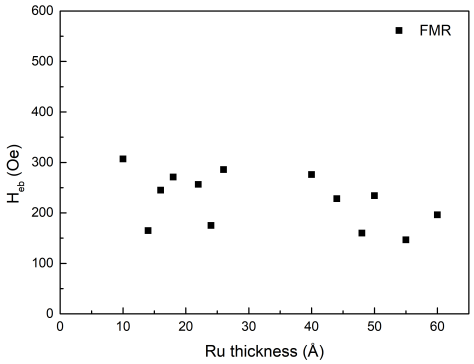

Figure 29 – H_{eb} Vs Ru thickness for Co.

and interdiffusion, can change the uncompensated spin density at the interface, also altering the bias (NASCIMENTO et al., 2013; MORALES et al., 2003). The exchange bias training effect can cause fluctuations as well by promoting a decrease in H_{eb} if measurements are not taken with identical field cycling history (BINEK, 2004; ZHENG et al., 2004). Considering these fluctuations as not being caused by magnetic interaction between the FM layers is corroborated by the agreement between the experimental data and the simulations, which did not consider any coupling between these layers.

Even if interlayer coupling is present, it is expected to be weak compared to the exchange bias at both interfaces and to predominantly affect the Py layer, owing to its softer ferromagnetic character. This behavior contrasts with that observed in IrMn/Py/-Ru/Co spin valves, in which the exchange bias field at the single AFM/FM interface clearly reflects the RKKY coupling between the ferromagnetic layers (ALAYO; BAGGIO-SAITOVITCH, 2010; TARAZONA et al., 2018). In both systems, magnetostatic "orange-peel" coupling can be ruled out, since the strength of this interaction decays exponentially with the Ru thickness. Overall, several factors may contribute to the cause of fluctuations in the exchange bias field.

The exchange bias field obtained from angular dependent FMR measurements , H_{eb}, can also be graphically defined as stated by equation 5.8 (GESHEV; PEREIRA; SCHMIDT, 2001; SOUSA, 2013).

$$H_{eb} = \frac{H_{res}(\pi) - H_{res}(0)}{2} \tag{5.8}$$

The values obtained for H_{eb} from the simulations are also consistent with the ones defined by equation 5.8 for both transitions of all samples. Therefore, in FMR experiments, analyzing the angular variation of the resonance field within the plane of the sample provides a direct way to estimate the exchange bias field. (SOUSA, 2013).

5.1.4 Gyromagnetic ratio and g-factor

Another parameter obtained by the simulations and fitting was the gyromagnetic ratio γ, which is related to the g-factor by

$$\gamma = -g\mu_B/\hbar. \tag{5.9}$$

The g-factor is defined as a proportionality constant relating the magnitude of the magnetic moment, measured in units of the Bohr magneton μ_B, to the magnitude of the angular momentum, measured in units of $\hbar$:

$$\frac{|m|}{\mu_B} = g\,\frac{|l|}{\hbar}. \tag{5.10}$$

Hence, for purely orbital motion, the g-factor is exactly equal to 1 and 2 for purely spin moments. The measured g typically deviates from 2.0 due to spin–orbit coupling, which mixes orbital angular momentum into the ground state (COEY, 2010). The g-factors of some metallic ferromagnets are shown in Table 5.1.4 and the g-factors determined by the simulations for both Py and Co modes are presented in Figure 30.

Fe	2,08
Co	2,17
Ni	2,18
Gd	1,95

Table 4 – g-factors for metallic ferromagnets (COEY, 2010).

The observed variation of the g-factor with the Ru spacer thickness, which exhibits an oscillatory component combined with a broader trend, may be explained by different physical phenomena that alter the effective spin-orbit coupling. Variations in interfacial strain or changes in growth morphology with increasing spacer thickness may systematically affect the local crystal field environment and spin-orbit interaction at the Co/Ru and Ru/Py interfaces.

5.2 Comparison to magnetization measurements

All of the magnetization measurements indicate a horizontally shifted hysteresis loop, which is a determinant feature of the exchange bias effect. Over 70% of the samples

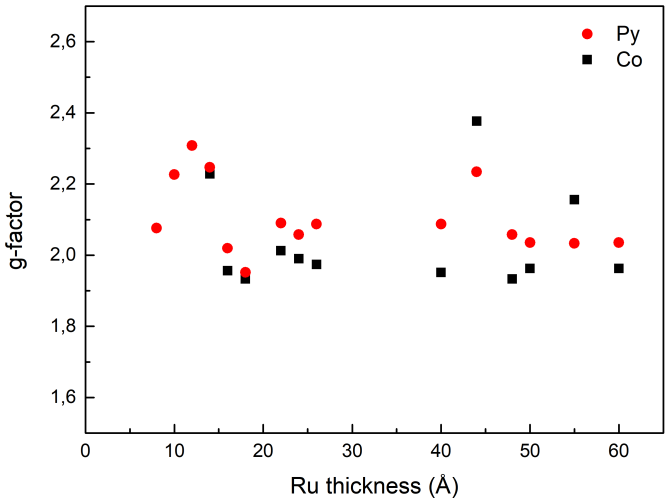

Figure 30 – g-factors Vs Ru thickness.

present subloops (Ru 10, 16, 18, 20, 22, 24, 28, 40, 48, 50, 55 and 60 Å), as in the hysteresis of the Ru 16 Å sample, shown in Figure 31, while the others demonstrate single-loop hysteresis (Ru 12, 26, 32 and 44 Å), similarly to the Ru 26 Å sample, shown in Figure 32. Notably, all samples except Ru 8 Å and Ru 14 Å are found to be saturated at external fields corresponding to the FMR resonance fields.

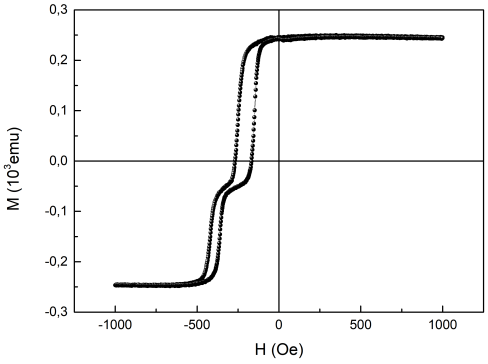

Figure 31 – Total magnetic moment for Ru 16 Å.

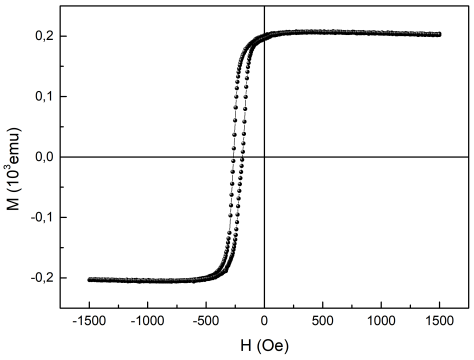

Figure 32 – Total magnetic moment for Ru 26 Å.

In a single-loop hysteresis, the exchange bias (EB) field is defined as the horizontal distance from the center of the loop to the origin. On the other hand, in a hysteresis with two subloops, each subloop corresponds to a ferromagnetic domain (or FM layer) in the sample that reverses individually. In this case, each subloop determines an EB field in a similar manner to the single-loop hysteresis. The height of each subloop can be used to identify to wich FM layer it corresponds, since this height should be proportional to the magnetization of the FM material (OLAMIT et al., 2005). In that sense, the top subloop

was attributed to the Co layer and the bottom one to the Py layer. For the samples with single-loop hysteresis, the EB field was attributed to the Co layer only.

The EB fields determined by the FMR technique and MxH measurements for the Py and Co layers are presented in Figures 33 and 34. These two values should, in general, give different values because different magnetization processes are involved in the hysteresis loop (quasi-static phenomenon) and FMR measurements (dynamic phenomenon). Consequently, the EB fields extracted from these techniques correspond to distinct physical quantities (GESHEV; PEREIRA; SCHMIDT, 2001). In spite of that, both fluctuate in the same field range.

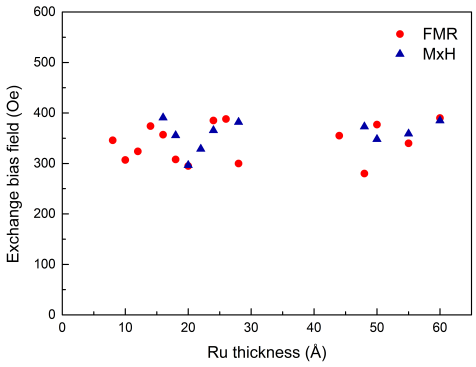

Figure 33 – Comparison of EB fields for Py.

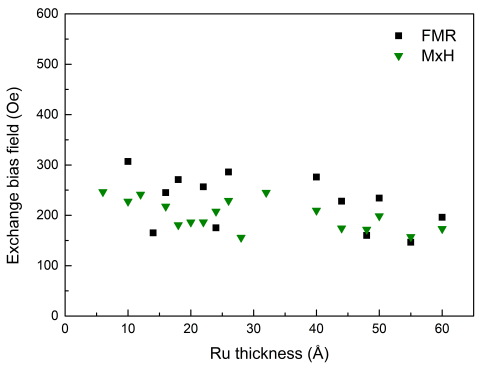

Figure 34 – Comparison of EB fields for Co.

Conclusions

This dissertation investigates the exchange bias effect in the IrMn/Co and Py/IrMn interfaces of Si/Ru/IrMn/Co/Ru/Py/IrMn/Ru multilayers produced by magnetron sputtering. The samples, which vary in the central ruthenium layer's thickness, were mainly characterized by ferromagnetic resonance (FMR) experiments performed at room temperature.

Ferromagnetic resonance (FMR) spectra were acquired for in-plane angular positions of the applied magnetic field ranging from 0 to 360 degrees. The spectra exhibit two well-defined resonance modes: the mode at higher resonance fields is associated with the Py layer, while the mode at lower resonance fields corresponds to the Co layer. All spectra were fitted using derivatives of Lorentzian functions, primarily in order to determine the resonance fields.

The analysis of the resonance field H_{res} of the Py and Co modes as a function of the field angle revealed a 360-degree periodicity, demonstrating the presence of unidirectional anisotropy in all films, in agreement with the expected exchange bias effect. The $H_{res} \times \phi$ curves were fitted by simulating the resonance conditions with the Smit-Suhl-Beljers approach, which obtains the resonance fields by minimizing the free energy density function of the film. For the system under study, the energy density of each ferromagnetic layer includes the Zeeman, demagnetization, uniaxial anisotropy, and the exchange bias energy terms. The simulation fittings revealed high correlation coefficients with respect to the experimental data and, from these simulations, the exchange bias field, uniaxial anisotropy field, magnetization, and g-factor of each resonant mode were obtained.

The values obtained for the exchange bias field H_{eb} are in accordance with the values determined from the graphic definition and with those determined from the magnetization measurements. They exhibit a non-monotonic trend with respect to the Ru layer's thickness, fluctuating about the mean value of 340 Oe for the IrMn/Py interface and 220 Oe for the Co/IrMn interface. These fluctuations can be explained by grain size distribution in the AFM layers, interface roughness and interdiffusion, as well as the exchange bias training effect. However, if these fluctuations are interpreted as presenting an oscillatory behavior, a possible explanation would be the RKKY interaction mediated by the nonmagnetic Ru layer, similar to what is observed in the IrMn/Py/Ru/Co spin valves. Regardless, this interaction should be weak compared to the exchange bias at both interfaces.

In light of the above, the results, in addition to showing that the exchange bias field in both FM/AFM interfaces fluctuates with Ru thickness, provide structural insight

on the samples and information on the electronic environment (revealed by the g-factor). This demonstrates the versatility and sensitivity of the FMR technique in the context of magnetic thin films. The results also have implications for the design of multilayers for spintronics applications, since understanding ways to control the exchange bias effect can lead to the development of different spintronics devices.

Building on the current analysis, it would be of interest to further investigate this system using Q-band FMR, as the higher frequency helps to separate overlapping resonance modes, improving the amount of resonance fields available for analysis. Another possibility would be to perform out-of-plane FMR measurements, with the external magnetic field applied perpendicularly to the film plane, in order to quantify the perpendicular magnetic anisotropy and study the interfacial anisotropies of each ferromagnetic layer independently. This geometry would also permit extraction of the perpendicular gyromagnetic ratio, offering a more complete magnetic characterization. Moreover, doing these experiments in lower temperatures (around 100 K) could reduce interactions originated from thermal fluctuation and enhance sensitivity to intrinsic magnetic coupling mechanisms, clarifying the relative contributions of thermal and structural effects to the observed behavior. Finally, another approach that could benefit the study of these kinds of systems would be to produce them by molecular beam epitaxy (MBE) instead of magnetron sputtering in order to decrease growth-related interface effects, such as interfacial roughness and interdiffusion.

Referências

ALAYO, W.; BAGGIO-SAITOVITCH, E. Study of the interlayer coupling and its temperature dependence in spin valves with ru and cu spacers. *Journal of Applied Physics*, AIP Publishing, v. 107, n. 7, 2010. Cited 3 times in pages 34, 56 e 57.

ALAYO, W. et al. Analysis of the weak coupling of the irmn/co/ru/nife structures by ferromagnetic resonance. *Journal of Applied Physics*, AIP Publishing, v. 109, n. 8, 2011. Cited 2 times in pages 51 e 54.

ALAYO, W.; XING, Y.; BAGGIO-SAITOVITCH, E. Magnetization studies in irmn/co/ru/nife spin valves with weak interlayer coupling. *Journal of Applied Physics*, AIP Publishing, v. 106, n. 11, 2009. Cited 3 times in pages 32, 34 e 52.

ASHCROFT, N. W.; MERMIN, N. D. Solid state physics (brooks cole, 1976). *Cited on*, v. 26, 1993. Cited in page 25.

BINEK, C. Training of the exchange-bias effect: A simple analytic approach. *Physical Review B—Condensed Matter and Materials Physics*, APS, v. 70, n. 1, p. 014421, 2004. Cited in page 57.

BLACHOWICZ, T.; EHRMANN, A. Exchange bias in thin films—an update. *Coatings*, MDPI, v. 11, n. 2, p. 122, 2021. Cited 2 times in pages 36 e 37.

BLUNDELL, S. *Magnetism in condensed matter*. [S.l.]: OUP Oxford, 2001. Cited 11 times in pages 20, 22, 23, 24, 25, 26, 27, 28, 29, 30 e 49.

BOBO, J.-F.; FISCHER, H.; PIECUCH, M. Modification of magnetic coupling in antiferromagnetically coupled bilayers due to the existence of ferromagnetic pin holes. *MRS Online Proceedings Library (OPL)*, Cambridge University Press, v. 313, p. 467, 1993. Cited in page 34.

BRÄUER, G. et al. Magnetron sputtering–milestones of 30 years. *Vacuum*, Elsevier, v. 84, n. 12, p. 1354–1359, 2010. Cited in page 45.

BRIGNETI, E. V. et al. Ferromagnetic resonance and magnetization in permalloy films with nanostructured antidot arrays of variable size. *Journal of Magnetism and Magnetic Materials*, Elsevier, v. 320, n. 14, p. e257–e260, 2008. Cited in page 54.

BUSCHOW, K. *Physics of Magnetism and Magnetic Materials*. [S.l.]: Springer US, 2003. Cited 5 times in pages 20, 21, 24, 28 e 30.

BUSCHOW, K. J. *Concise encyclopedia of magnetic and superconducting materials*. [S.l.]: Elsevier, 2005. Cited 4 times in pages 28, 33, 34 e 35.

CHOO, D. et al. A model of the magnetic properties of coupled ferromagnetic/ antiferromagnetic bilayers. *Journal of applied physics*, AIP Publishing, v. 101, n. 9, 2007. Cited in page 38.

COEY, J. M. *Magnetism and magnetic materials*. [S.l.]: Cambridge university press, 2010. Cited 15 times in pages 9, 10, 20, 22, 24, 25, 26, 27, 29, 30, 34, 35, 39, 40 e 58.

Collins Dictionary. *Hysteresis*. 2024. Accessed: 29 January 2026. Disponível em: <https://www.collinsdictionary.com>. Cited in page 22.

CULLITY, B. D.; GRAHAM, C. D. *Introduction to magnetic materials*. [S.l.]: John Wiley & Sons, 2011. Cited in page 29.

DIMITRIADIS, V. et al. Shape-dependent exchange bias effect in magnetic nanoparticles with core-shell morphology. *Physical Review B*, APS, v. 92, n. 6, p. 064420, 2015. Cited in page 38.

DONG, Y. et al. Room temperature manipulation of exchange bias in magnetic heterojunctions. *Journal of Magnetism and Magnetic Materials*, Elsevier, v. 559, p. 169546, 2022. Cited in page 17.

ENNEN, I. et al. Giant magnetoresistance: Basic concepts, microstructure, magnetic interactions and applications. *Sensors*, MDPI, v. 16, n. 6, p. 904, 2016. Cited in page 17.

FAN, Y. et al. Programmable spin–orbit torque multistate memory and spin logic cell. *ACS nano*, ACS Publications, v. 16, n. 4, p. 6878–6885, 2022. Cited in page 17.

FARLE, M. Ferromagnetic resonance of ultrathin metallic layers. *Reports on progress in physics*, IOP Publishing, v. 61, n. 7, p. 755, 1998. Cited 6 times in pages 28, 31, 33, 39, 51 e 54.

GESHEV, J.; PEREIRA, L. G.; SCHMIDT, J. E. Angular dependence of the exchange bias obtained from magnetization and ferromagnetic resonance measurements in exchange-coupled bilayers. *Physical Review B*, APS, v. 64, n. 18, p. 184411, 2001. Cited 3 times in pages 52, 57 e 60.

GLOANEC, M. et al. Temperature dependence of exchange bias in nife/femn bilayers. *Physical Review B—Condensed Matter and Materials Physics*, APS, v. 82, n. 14, p. 144433, 2010. Cited in page 51.

GREENE, J. E. Tracing the 5000-year recorded history of inorganic thin films from 3000 bc to the early 1900s ad. *Applied Physics Reviews*, AIP Publishing, v. 1, n. 4, 2014. Cited in page 17.

GRÜNBERG, P. Layered magnetic structures: History, highlights, applications. *Physics Today*, AIP Publishing, v. 54, n. 5, p. 31–37, 2001. Cited in page 33.

GUIMARÃES, A. P.; OLIVEIRA, I. S. Magnetism and magnetic resonance in solids. *(No Title)*, 1998. Cited 5 times in pages 21, 22, 23, 24 e 39.

HARRES, A.; GESHEV, J. A polycrystalline model for magnetic exchange bias. *Journal of Physics: Condensed Matter*, IOP Publishing, v. 24, n. 32, p. 326004, 2012. Cited in page 38.

HEINRICH, B.; COCHRAN, J. Ultrathin metallic magnetic films: magnetic anisotropies and exchange interactions. *Advances in Physics*, Taylor & Francis, v. 42, n. 5, p. 523–639, 1993. Cited in page 34.

HUANG, J. et al. Double-exchange bias modulation under horizontal and perpendicular field directions by 3d nanocomposite design. *ACS Applied Materials & Interfaces*, ACS Publications, v. 13, n. 42, p. 50141–50148, 2021. Cited in page 17.

HUANG, X. et al. Manipulating exchange bias in 2d magnetic heterojunction for high-performance robust memory applications. *Nature Communications*, Nature Publishing Group UK London, v. 14, n. 1, p. 2190, 2023. Cited in page 17.

IGLESIAS, O.; LABARTA, A.; BATLLE, X. Exchange bias phenomenology and models of core/shell nanoparticles. *Journal of nanoscience and nanotechnology*, American Scientific Publishers, v. 8, n. 6, p. 2761–2780, 2008. Cited in page 38.

JOHNSON, M. et al. Magnetic anisotropy in metallic multilayers. *Reports on Progress in Physics*, IOP Publishing, v. 59, n. 11, p. 1409, 1996. Cited 5 times in pages 9, 28, 31, 32 e 33.

KELLY, P. J.; ARNELL, R. D. Magnetron sputtering: a review of recent developments and applications. *Vacuum*, Elsevier, v. 56, n. 3, p. 159–172, 2000. Cited in page 45.

KIWI, M. Exchange bias theory. *Journal of Magnetism and Magnetic materials*, Elsevier, v. 234, n. 3, p. 584–595, 2001. Cited 4 times in pages 9, 35, 36 e 37.

KIWI, M. et al. Positive exchange bias model: Fe/fef2 and fe/mnf2 bilayers. *Solid state communications*, Elsevier, v. 116, n. 6, p. 315–319, 2000. Cited in page 37.

KIWI, M. et al. Exchange-bias systems with compensated interfaces. *Applied Physics Letters*, American Institute of Physics, v. 75, n. 25, p. 3995–3997, 1999. Cited in page 37.

LINDNER, J.; BABERSCHKE, K. In situ ferromagnetic resonance: an ultimate tool to investigate the coupling in ultrathin magnetic films. *Journal of Physics: Condensed Matter*, IOP Publishing, v. 15, n. 4, p. R193, 2003. Cited 4 times in pages 17, 39, 41 e 49.

MALOZEMOFF, A. Random-field model of exchange anisotropy at rough ferromagnetic-antiferromagnetic interfaces. *Physical review B*, APS, v. 35, n. 7, p. 3679, 1987. Cited in page 37.

MARKÓ, D. Magnetism in solids: hysteresis. In: *Reference module in materials science and materials engineering*. [S.l.]: Elsevier, 2018. Cited in page 22.

MATHON, J. Theory of magnetic multilayers. exchange interactions and transport properties. *Journal of magnetism and magnetic materials*, Elsevier, v. 100, n. 1-3, p. 527–543, 1991. Cited in page 34.

MAURI, D. et al. Simple model for thin ferromagnetic films exchange coupled to an antiferromagnetic substrate. *Journal of Applied Physics*, v. 62, n. 7, p. 3047–3049, 1987. Cited 3 times in pages 9, 37 e 38.

MEIKLEJOHN, W. Exchange anisotropy—a review. *Journal of Applied Physics*, American Institute of Physics, v. 33, n. 3, p. 1328–1335, 1962. Cited in page 36.

MERKEL, M. et al. Polycrystalline exchange-biased bilayers: Magnetically effective versus structural antiferromagnetic grain volume distribution. *Physical Review B*, APS, v. 106, n. 1, p. 014403, 2022. Cited in page 56.

MORALES, E. H. et al. Interdiffusion and exchange bias in the mn x pt 1- x/co system. *Journal of applied physics*, American Institute of Physics, v. 93, n. 8, p. 4729–4733, 2003. Cited in page 57.

MORALES, R. et al. Exchange-bias phenomenon: the role of the ferromagnetic spin structure. *Physical Review Letters*, APS, v. 114, n. 9, p. 097202, 2015. Cited in page 37.

MORITZ, J. et al. Orange peel coupling in multilayers with perpendicular magnetic anisotropy: Application to (co/pt)-based exchange-biased spin-valves. *Europhysics Letters*, IOP Publishing, v. 65, n. 1, p. 123, 2004. Cited in page 34.

MOSER, A. et al. Magnetic recording: advancing into the future. *Journal of Physics D: Applied Physics*, IOP Publishing, v. 35, n. 19, p. R157, 2002. Cited in page 17.

MYDOSH, J. A. *Spin glasses: an experimental introduction*. [S.l.]: CRC press, 1993. Cited 2 times in pages 26 e 27.

NASCIMENTO, V. et al. Clarifying roughness and atomic diffusion contributions to the interface broadening in exchange-biased nife/femn/nife heterostructures. *Thin solid films*, Elsevier, v. 542, p. 360–367, 2013. Cited in page 57.

NÉEL, L. Étude théorique du couplage ferro-antiferromagnétique dans les couches minces. In: *Annales de Physique*. [S.l.: s.n.], 1967. v. 14, n. 2, p. 61–80. Cited in page 36.

NOGUÉS, J.; SCHULLER, I. K. Exchange bias. *Journal of Magnetism and Magnetic Materials*, Elsevier, v. 192, n. 2, p. 203–232, 1999. Cited 4 times in pages 9, 34, 35 e 36.

OHRING, M. *Materials science of thin films: depositon and structure*. [S.l.]: Elsevier, 2001. Cited 2 times in pages 17 e 29.

OLAMIT, J. et al. Loop bifurcation and magnetization rotation in exchange-biased ni/fef 2. *Physical Review B—Condensed Matter and Materials Physics*, APS, v. 72, n. 1, p. 012408, 2005. Cited in page 59.

O'GRADY, K.; FERNANDEZ-OUTON, L.; VALLEJO-FERNANDEZ, G. A new paradigm for exchange bias in polycrystalline thin films. *Journal of Magnetism and Magnetic materials*, Elsevier, v. 322, n. 8, p. 883–899, 2010. Cited in page 38.

PESSOA, M. S. Anisotropia magnética em tricamadas epitaxiais fe/mn/fe. 2010. Cited 3 times in pages 31, 33 e 51.

POLISHCHUK, D. et al. Oscillatory exchange bias controlled by rkky in magnetic multilayers. *Applied Physics Letters*, AIP Publishing, v. 122, n. 6, 2023. Cited in page 56.

POULOPOULOS, P.; BABERSCHKE, K. Magnetism in thin films. *Journal of Physics: Condensed Matter*, IOP Publishing, v. 11, n. 48, p. 9495, 1999. Cited 3 times in pages 9, 28 e 29.

RADU, F. et al. Quantitative description of the azimuthal dependence of the exchange bias effect. *Journal of Physics: Condensed Matter*, IOP Publishing, v. 18, n. 3, p. L29, 2005. Cited in page 38.

SAHA, J.; VICTORA, R. H. Large scale micromagnetic simulation for the exchange interaction between a polycrystalline antiferromagnet and a ferromagnet. *Physical Review B—Condensed Matter and Materials Physics*, APS, v. 73, n. 10, p. 104433, 2006. Cited in page 38.

SCHMOOL, D. S. et al. Ferromagnetic resonance studies in magnetic nanosystems. *Magnetochemistry*, MDPI, v. 7, n. 9, p. 126, 2021. Cited in page 39.

SCHOLL, A. et al. Domain-size-dependent exchange bias in co/ lafeo3. *Applied physics letters*, AIP Publishing, v. 85, n. 18, p. 4085–4087, 2004. Cited in page 56.

SCHULTHESS, T.; BUTLER, W. Consequences of spin-flop coupling in exchange biased films. *Physical review letters*, APS, v. 81, n. 20, p. 4516, 1998. Cited in page 37.

SCHULTHESS, T.; BUTLER, W. Coupling mechanisms in exchange biased films. *Journal of Applied Physics*, American Institute of Physics, v. 85, n. 8, p. 5510–5515, 1999. Cited in page 37.

SMIT, J.; BELJERS, H. Philips res. rep. *Rep*, v. 1, n. 0, p. 113, 1955. Cited in page 40.

SOUSA, M. A. d. Estudo do fenômeno de exchange bias em bicamadas nife/irmn e tricamadas nife/irmn/co. 2013. Cited 5 times in pages 17, 51, 54, 57 e 58.

SOVSKII, S. V. V. *Ferromagnetic resonance: the phenomenon of resonant absorption of a high-frequency magnetic field in ferromagnetic substances*. [S.l.]: Elsevier, 2016. Cited 3 times in pages 9, 39 e 40.

STILES, M. D.; MCMICHAEL, R. D. Model for exchange bias in polycrystalline ferromagnet-antiferromagnet bilayers. *Physical Review B*, APS, v. 59, n. 5, p. 3722, 1999. Cited in page 38.

SUHL, H. Ferromagnetic resonance in nickel ferrite between one and two kilomegacycles. *Physical Review*, APS, v. 97, n. 2, p. 555, 1955. Cited in page 40.

SUN, Y. et al. Large and robust exchange bias in co/coo film: Implication for flexible spintronics. *Advanced Physics Research*, Wiley Online Library, v. 2, n. 1, p. 2200066, 2023. Cited in page 17.

TARAZONA, H. et al. Effect of the strong coupling on the exchange bias field in irmn/py/ru/co spin valves. *Journal of Magnetism and Magnetic Materials*, Elsevier, v. 446, p. 44–48, 2018. Cited in page 57.

WEBER, R. T. Xenon user's guide. *Bruker BioSpin Corporation, Billerica, MA USA*, 2011. Cited 3 times in pages 9, 47 e 48.

WEI, Y. *Ferromagnetic resonance as a probe of magnetization dynamics: A study of FeCo thin films and trilayers*. Tese (Doutorado) — Acta Universitatis Upsaliensis, 2015. Cited 12 times in pages 9, 20, 22, 23, 24, 27, 30, 31, 32, 34, 40 e 41.

WIGEN, P. E.; ZHANG, Z. Ferromagnetic resonance in coupled magnetic multilayer systems. *Braz. J. Phys*, v. 22, p. 267, 1992. Cited 2 times in pages 9 e 43.

YALÇIN, O. *Ferromagnetic resonance: theory and applications*. [S.l.]: BoD–Books on Demand, 2013. Cited 2 times in pages 39 e 40.

ZHANG, T.; DRESSEL, M. Grain-size effects on the charge ordering and exchange bias in pr 0.5 ca 0.5 mno 3: The role of spin configuration. *Physical Review B—Condensed Matter and Materials Physics*, APS, v. 80, n. 1, p. 014435, 2009. Cited in page 56.

ZHENG, R. et al. Training effect of exchange bias in γ-fe 2 o 3 coated fe nanoparticles. *Physical Review B—Condensed Matter and Materials Physics*, APS, v. 69, n. 21, p. 214431, 2004. Cited in page 57.

Apêndices

APÊNDICE A – Maple coding for Smit-Suhl-Beljers approach

This appendix presents the Maple 2015 code used in the numerical calculations of Smit-Suhl-Beljers approach and simulations for the FMR angular dependence of resonance fields. The routines are included to document the computational steps involved in data fitting and model evaluation, allowing interested readers to reproduce or adapt the procedures.

```
restart; with(plots); with(Optimization);
interface(prettyprint = 0);  Digits := 15;
unprotect(GAMMA);

dados_Y := [462.70876, 475.54217, ... , 554.00555];
dados_X := [0, 20, 40, ... , 360];

N := nops(dados_X);

w := 2*Pi*0.950e10;
phiafmi := 0.1;
M := 800;    He := 230;    Hu := 5.0;
GAMMA := 18266106.;
unassign('M_', 'He_', 'Hu_', 'Gamma_', 'phiafmi_');
```

Listing A.1 – Initialization of Maple environment and experimental data.

```
Fsym := M_*(-H*sin(theta)*cos(phih-phi)
            + 2*Pi*M_*cos(theta)^2
            - 0.5*Hu_*sin(theta)^2*cos(phi)^2
            - He_*sin(theta)*cos(phi - phiAF_));

F1sym  := diff(Fsym, theta);
F2sym  := diff(Fsym, phi);
F11sym := diff(F1sym, theta);
F22sym := diff(F2sym, phi);
F12sym := diff(F1sym, phi);
```

```
11
12 Rsym := sqrt(F11sym*F22sym - F12sym^2)/(M_*sin(theta))
13           - w/Gamma_;
```

Listing A.2 – Free energy density and symbolic derivatives.

```
1  Simula := proc(Mloc, Gammaloc, Heloc, Hwloc, Huloc, phiAF_loc)
2      local i, phi1, eps, Hsim_local, Fp1, Fp2, Rp,
3            sol, ok, Hprev, phiprev, thetaprev, thmid,
4            dth, Hmax;
5
6      eps := 0.10e-4;  Hmax := 4500.0;
7      thmid := Pi/2;   dth := .60;
8
9      Hsim_local := Array(1..N, fill = Float(undefined));
10     Hprev := NULL;  phiprev := NULL;  thetaprev := NULL;
11
12     for i to N do
13         phi1 := dados_X[i]*Pi/180.0;
14
15         Fp1 := eval(F1sym, [...] );
16         Fp2 := eval(F2sym, [...] );
17         Rp  := eval(Rsym, [...] );
18
19         ok := false;
20
21         # Attempt 1: use previous solution as initial guess
22         if Hprev <> NULL then
23             try sol := fsolve({Fp1=0, Fp2=0, Rp=0},
24                               {H=Hprev, phi=phiprev, theta=
    thetaprev});
25                 if type(sol,set) and has(sol,H) then ok := true
    end if;
26             catch: ok := false end try;
27         end if;
28
29         # Attempt 2: fixed initial guess
30         if not ok then
31             try sol := fsolve({Fp1=0, Fp2=0, Rp=0},
32                               {H=1000., phi=phi1, theta=thmid});
33                 if type(sol,set) and has(sol,H) then ok := true
```

```
    end if;
34              catch: ok := false end try;
35          end if;
36
37          # Attempt 3: fully bounded search
38          if not ok then
39              try sol := fsolve({Fp1=0, Fp2=0, Rp=0},
40                                {H,phi,theta},
41                                H=0..Hmax, phi=0..2*Pi,
42                                theta=thmid-dth..thmid+dth);
43                  if type(sol,set) and has(sol,H) then ok := true
    end if;
44              catch: ok := false end try;
45          end if;
46
47          if ok then
48              Hsim_local[i] := evalf(eval(H,sol));
49              Hprev := evalf(eval(H,sol));
50              phiprev := evalf(eval(phi,sol));
51              thetaprev := evalf(eval(theta,sol));
52          else
53              Hsim_local[i] := Float(undefined);
54              Hprev := NULL; phiprev := NULL; thetaprev := NULL;
55          end if;
56
57      end do;
58
59      return Hsim_local;
60  end proc;
```

Listing A.3 – Simulation procedure to compute the resonance field.

```
1  H_sim0 := Simula(M, GAMMA, He, Hw, Hu, phiafmi);
2
3  Pexp  := pointplot([...], color=red, symbol=solidcircle);
4  Psim0 := pointplot([...], color=blue, symbol=solidcircle);
5
6  display([Pexp, Psim0],
7          labels=["phi_h (deg)", "Hres (Oe)"],
8          title="Experimental vs Simulated (initial)");
```

Listing A.4 – Plot of experimental data and initial simulation.

```
SSEeval := proc(Mv, Gv, Hev, Hwv, Huv, phiAFv)
    local Hfit, i, r, s, del, res;

    Hfit := Simula(Mv, Gv, Hev, Hwv, Huv, phiAFv);
    del := 80.0;  s := 0.;

    for i to N do
        if type(Hfit[i],float) then
            r := Hfit[i] - dados_Y[i];
            res := `if`(abs(r)<=del, .5*r*r, del*(abs(r)-.5*del))
   ;
            s := s + res;
        else
            s := s + 0.5e8;
        end if;
    end do;

    return s;
end proc;
```

Listing A.5 – Objective function for nonlinear fitting.

```
f := proc(x)
    local Mv, Hev, Huv, Gv, pAv, val;
    try
        Mv := evalf(x[1]);  Hev := evalf(x[2]);
        Huv := evalf(x[3]); Gv := evalf(x[4]);
        pAv := evalf(x[5]);
        val := SSEeval(Mv, Gv, Hev, Hw, Huv, pAv);
        if not type(val,numeric) then return 0.10e13 end if;
        return val;
    catch:
        return 0.10e13;
    end try;
end proc;

init_vals := [M, He, Hu, GAMMA, phiafmi];
bnds := [[400.,1200.], [-800.,800.], [-400.,400.],
         [0.12e8,0.26e8], [-.6,.6]];

```

```
# coarse grid search (omitted here for brevity)
# ...

# nonlinear simplex
xopt := NULL; SSEop := NULL;

try
    xopt, SSEop := Optimization:-NLPSolve(
                        f,
                        bestx,
                        bounds = bnds,
                        method = nonlinearsimplex,
                        evaluationlimit = 12000,
                        iterationlimit = 2500) ;
    catch: printf("NLPSolve falhou (excecao capturada). Mantendo
   bestx.\n")
end try
```

Listing A.6 – Parameter search and nonlinear optimization.

```

best_final := bestx; best_val := bestv;

if (type(xopt, list) or type(xopt, Vector)) then
    if not (type(SSEop, numeric)) then SSEop := f(xopt) end if;
    if type (type(SSEop, numeric) and SSEop < best_val) then
        best_final := [xopt[1], xopt[2], xopt[3], xopt[4], xopt
   [5]];
        best_val := SSEop end if end if;
        printf("SSE (escolhido) = %.6g\n", best_val);


M := best_final[1];
He := best_final[2];
Hu := best_final[3];
GAMMA := best_final[4];
phiafmi := best_final[5];

unassign('H', 'phi', 'theta');
forget(Simula)

```

```
21
22 H_fit := Simula(M, GAMMA, He, Hw, Hu, phiafmi);
23
24 Pfit := pointplot([...], connect=true, color=blue);
25
26 display([Pexp, Pfit],
27         labels=["phi_h (deg)", "Hres (Oe)"],
28         title=sprintf("Best fit: M=%.1f, He=%.1f, ...", M,He));
29
30 # CSV table
31 fname := "tabela_ajuste.csv";
32 F := fopen(fname, WRITE, TEXT);
33 fprintf(F, "phi_h_deg,Hres_fit_Oe\n");
34
35 for i to N do
36     fprintf(F, "%g,%g\n", dados_X[i], H_fit[i]);
37 end do;
38
39 fclose(F);
```

Listing A.7 – Final best fit and CSV export.